Received: 28 February 2025 | Revised: 7 August 2025 | Accepted: 8 September 2025

DOI: 10.1002/qj.70042

Quarterly Journal of the Royal Meteorological Society RMetS

RESEARCH ARTICLE

# Evaluation of the WRF model for simulating deep convection and cold-pool characteristics relevant to wind-energy applications in Germany

**Gerard Kilroy** | **Jeffrey D. Thayer**

German Aerospace Center (DLR), Institute of Atmospheric Physics, Oberpfaffenhofen, Germany

**Correspondence**
Gerard Kilroy, German Aerospace Center (DLR), Institute of Atmospheric Physics, Oberpfaffenhofen, Germany.
Email: gerard.kilroy@dlr.de

**Funding information**
Deutsches Zentrum fur Luft- und Raumfahrt DLR

## Abstract

Deep convection and cold-pool characteristics over Germany during July 2023 are investigated using Deutscher Wetterdienst (DWD) radar observations and a convection-permitting Weather Research and Forecasting (WRF) model simulation. The analysis combines instantaneous snapshots of convection with a Lagrangian tracking approach to examine the life cycles of isolated convective cells. WRF successfully captures the general morphology and evolution of deep convection and associated cold pools, although it tends to produce smaller, more intense rain-producing cells. Simulated cold-pool properties-including wind gusts and virtual potential temperature ($\theta_v$) reductions-align well with observations (e.g., median $\theta_v$ drop of $-2.95\,K$ and wind gusts of $4.28\ m \cdot s^{-1}$, extreme gusts of $> 10\,m \cdot s^{-1}$), suggesting that the model represents key features of convective outflows reliably. The temporal evolution of convective cell properties shows a downward-facing parabolic pattern in both model and observations in terms of cell size, rain rate, and reflectivity, although WRF intensifies convection too quickly and consistently overestimates rain rates. An analysis of wind-energy-relevant metrics reveals that cold pools induce substantial increases in wind speed, stability, and vertical shear. Estimated power output increases by 35%–60% for long-lived cells and 33%–50% for short-lived ones, peaking during the mid-to-late cell life cycle. These findings highlight the need to consider cold-pool dynamics in wind-energy forecasting and operations.

**KEYWORDS**

cold pool, deep convection, Germany, wind energy, wind gusts, WRF model

## 1 | INTRODUCTION

As the contribution of wind energy increases in the German energy grid (from 1.7% in 2000 to 34% over the first half of 2024: BMWK, 2024; Fraunhofer ISE, 2024), it is becoming increasingly important to attain a more complete understanding of meteorological phenomena that impact wind-energy production. While larger-scale events, such as cold fronts, mesoscale storms, or low-level jets (DeMarco & Basu, 2018) can lead to dramatic changes in

energy output, they are relatively easy to forecast and prepare for in advance. Events that occur on shorter time scales and smaller spatial scales, which can be associated with rapid changes in wind speed and direction, are much harder to predict. So-called "wind ramps" can be associated with a variety of meteorological events and present issues for electrical system stability, while also contributing to forecasting errors (Feng & Zhang, 2018; Gallego *et al.*, 2015). Wind ramps associated with deep convection (Canepa *et al.*, 2020; Drew *et al.*, 2018; Steiner *et al.*, 2017) are particularly difficult to predict, due to the intrinsically stochastic nature of deep convection.

Deep convective clouds (or thunderstorms) are associated with multiple extreme weather phenomena, including lightning, hail, abrupt darkening, heavy precipitation, and rapid changes in wind speed and direction (wind ramps). Convectively induced wind ramps, also known as cold-pool "gust fronts", play an important role in wind-energy applications, particularly in the context of wind turbine performance and longevity. These cold pools form when cold, denser air produced within thunderstorms spreads out near the surface (Benjamin, 1968; Droegemeier & Wilhelmson, 1987). This denser, cooler air is produced primarily by the evaporative cooling of precipitation and the melting of ice hydrometeors, while hydrometeor loading also contributes to the downward acceleration of air (Zipser, 1969). Cold-pool gust fronts also impose increased mechanical loads on wind turbines, as the sudden changes in wind speed and direction can stress turbine blades (Kelly *et al.*, 2021).

Deep-convection-induced gust fronts play an important role in producing minute-scale fluctuations in wind-energy output (Pichault *et al.*, 2022). In particular, the strongest winds associated with cold-pool gust fronts can typically occur at around 100-m height above ground (Canepa *et al.*, 2020; Goff, 1976; Gunter & Schroeder, 2015; Lombardo *et al.*, 2014), which is usually close to hub height for onshore wind turbines (BWE, 2023). The gust front initially leads to a temporary increase in wind speeds and increased energy production, but following the gust front passage there are reduced winds and a temporary stabilization of the boundary layer. This stabilization can last approximately two hours (Kruse *et al.*, 2022) and affects the strength and duration of the turbine-induced turbulent wake (Englberger & Doernback, 2018). Due to the relatively small scale of individual single-cell thunderstorms, which can be just a few kilometres in diameter (Houze, 2014), and due to the non-stationary short-lived nature of convection (Goudenhpofdt & Delobbe, 2013), there are difficulties in capturing cold-pool characteristics.

Cold pools are relatively rare events, occurring only between 24 and 44 times per summer season (as, for example, observed in Hamburg with mast data: Kirsch *et al.*, 2021), with a typical maximum occurrence in July (Kirsch *et al.*, 2021; Pacey *et al.*, 2021). Due to the relative paucity of these events and the lack of an extensive ground-based observational network, there is a need to acquire comprehensive statistics on cold-pool events. One such observational field campaign, the Field Experiment on Sub-mesoscale Spatio-Temporal Variability in Lindenberg (FESSTVaL: Hohenegger *et al.*, 2023), attempted to capture cold-pool characteristics by employing a dense observation network of more than 100 stations with near-surface measurements during the summer months of 2021. From data obtained during this campaign, Kirsch *et al.* (2024) investigated the morphology of convective cold pools (size, shape, and structure), as well as factors controlling their growth using surface-based observations. They found that cold pools are far from circular in shape, having aspect ratios between 1.5 and 1.6 independent of their size and strength, which is likely due to the propagation of parent rainfall cells stretching the associated cold pools along the direction of the background flow (Parker, 1996). They found a median temperature difference, or cold-pool strength, of about −4 K, which is similar to other studies in Hamburg (Kirsch *et al.*, 2021) and the Netherlands (Kruse *et al.*, 2022). Extreme cases of up to −10.8 K have been observed (Kirsch *et al.*, 2021). The passing of a cold pool is characterized not only by a steep decrease in temperature, but also by a wind-speed perturbation of the order of a few metres per second (Kruse *et al.*, 2022 found a median wind anomaly of 4.4 $m \cdot s^{-1}$).

Ground-based observation networks can provide important insight into convective cold pools that affect a fixed location; however, there is often information lacking, including the three-dimensional structure and temporal evolution of cold-pool and parent-cell attributes. An attempt to characterize deep-convective life cycles, including the lifetime, size, and intensity development of storms, was performed by Wilhelm *et al.* (2023) using the detection and tracking algorithm KONvektive Entwicklung in RADarprodukten (KONRAD) developed at the German Meteorological Service (Deutscher Wetterdienst: DWD). In particular, they focused on life cycles of convective cells in Germany, analysing isolated convective storms for the summer periods from 2011 to 2016. They found that "an axially symmetric parabola opened downwards describes the mean cell area evolution well", with longer-lived cells having larger areas. They also showed that higher thermal instability is associated with faster initial growth, and the initial growth of the cell (in the first 5–35 minutes of the life cycle) provides the best skill in predicting whether a cell has a short or long lifetime, and thus a small or large lifetime maximum area. Wapler (2021) performed a similar multi-year analysis of convective storms and showed that the average temporal evolution of the storm size is

symmetric, with the maximum being reached halfway through the cell lifetime.

Observational studies seldom offer insights into the three-dimensional structure of convective cells and cold pools as they evolve over time. One method to overcome these deficiencies is to use numerical models to compliment ground-based and radar-derived observations to obtain a more complete understanding. Grant *et al.* (2024) performed such a study using the Icosahedral Nonhydrostatic model in large-eddy-simulation mode (ICON-LES) over Germany and found that the model underestimated the observed cold-pool temperature variability substantially (compared with the FESSTVaL observations), even when the mean cold-pool properties are well represented. The Weather Research and Forecasting (WRF) model has previously been used to gain an understanding of convection characteristics over Germany. Wagner *et al.* (2018a) showed that WRF is generally able to represent the diurnal cycle, structure, and intensity distribution of precipitation when compared with DWD observational datasets. However, the chosen WRF model setup can lead to significantly varied results. In particular, the choice of the cloud microphysics scheme in WRF has been shown to impact the properties of convection significantly (Fan *et al.*, 2017; Anisomiv *et al.*, 2023; Pandey *et al.*, 2023). In some cases, the model tends to exhibit a positive bias in terms of high rain rate (Pryor *et al.*, 2023), while in others the model underestimates total stratiform precipitation (Han *et al.*, 2019). Putnam *et al.* (2016) compared WRF simulations of a mesoscale convective system and a supercell when implementing five different microphysics schemes. All schemes investigated underestimated liquid water content in regions of pure rain, with some schemes producing too much graupel and others showing a small raindrop bias. Similarly, Köcher *et al.* (2023) compared five different schemes and found that the WRF model is generally unable to simulate extreme hail events over southern Germany.

Of the available microphysics schemes well suited for simulating deep convection and associated cold pools, the WRF Double-Moment 6-class (WDM6) microphysical scheme (Lim & Hong, 2010) has been given particular attention in the literature. While some studies have shown that this scheme produces excessively high concentrations of small-to-medium raindrops (Putnam *et al.*, 2016; Zhuo *et al.*, 2022) and may underestimate the extent of stratiform precipitation-potentially leading to an underestimation of convective area, cold-pool size, and strength-other studies suggest it performs well in simulating the inner core regions of convective cells. For a simulated mesoscale convective system, Wise *et al.* (2024) found that the WDM6 microphysics scheme produces a rain water mixing-ratio profile that decreases sharply below the cloud base, in contrast to the relatively uniform profiles produced by the commonly used Thompson (Thompson *et al.*, 2008) and Morrison (Morrison *et al.*, 2009) schemes. This sharper decline leads to enhanced evaporative cooling, resulting in a stronger cold pool and associated gust front. In bow-echo simulations, however, Zhuo *et al.* (2022) found that all three of these schemes underestimate cold-pool strength by about 25%. These studies suggest that there is some disagreement on the performance of the WDM6 microphysics scheme depending on the type of convection organization being simulated; however, in terms of deep convection generally, this scheme has shown better agreement with radar observations (Min *et al.*, 2015) and can produce more realistic vertical cell structure (Song & Sohn, 2018). Moreover, recent studies suggest a more realistic representation of cold-pool structure and strength (Anisomiv *et al.*, 2023; Wise *et al.*, 2024), which motivates our selection of WDM6 herein.

As far as we are aware, an evaluation of simulated deep convection and associated cold pools with a focus on wind-energy-relevant quantities has not yet been performed. A deeper understanding of convective cold pools and their parent cells in the context of wind energy would enable wind-farm operators to be more aware of the impacts of cold-pool gust fronts and optimize turbine operations accordingly. There remains limited understanding of the temporal evolution of cold-pool properties, such as strength, size, depth, and lifetime evolution. To this end, we evaluate simulated characteristics of deep convection by comparing a WRF simulation with DWD radar observations. A statistical evaluation of the convection produced by the model is required before the suitability of the model in simulating cold pools near the surface, where observations are sparse, can be addressed. Thereafter, we provide general guidance on potential cold-pool gust-front effects relevant to wind energy. The key questions addressed in this work are as follows.

- To what extent can WRF reproduce the bulk observed convection characteristics in Germany?
- How much do the wind, temperature, and temperature stratification change during simulated convective cold-pool passage?
- How do convective cold-pool characteristics relevant for wind energy evolve through a typical convective cell life cycle?
- Are convective cold pools a significant factor for wind-energy applications?

The simulation performed in this study is evaluated, where possible, using weather radar measurements supplied by DWD. The remainder of the article is organized

as follows. In Section 2, the model setup, datasets, and methodology are described. In Section 3, modelled convective cell characteristics are compared with DWD observations, while in Section 4 aspects of convection related to wind energy are explored. Convection and cold-pool life cycles are investigated in Section 5, while the conclusions are given in Section 6.

## 2 | NUMERICAL MODEL, DATASETS, AND METHODOLOGY

### 2.1 | WRF model setup

The simulation presented in this study is conducted using WRF (V4.4.1), a state-of-the-art, non-hydrostatic model widely utilized in the meteorological community for both operational forecasting and research purposes (Skamarock *et al.*, 2021). This model solves the fully compressible Euler equations, employing a terrain-following, hybrid sigma-pressure vertical coordinate system. The numerical model configuration for this simulation features two nested domains with horizontal resolutions of 5 km and 1 km. The horizontal grid dimensions are 300 × 300 for Domain 1 (D1) and 901 × 901 for Domain 2. The innermost domain (D2) incorporates 57 vertical levels. Vertical nesting is also applied, ensuring that the inner domain with finer horizontal resolution has higher vertical resolution. The lowest kilometre above ground level contains approximately 6–8 full model levels, depending on the terrain. This corresponds to a vertical grid spacing of roughly 100–150 m in the boundary layer, with even finer spacing closer to the surface. Initial and boundary conditions are supplied from the European Centre for Medium-Range Weather Forecasts (ECMWF) operational analyses, provided every six hours. The model's top boundary is set at a height corresponding to 50 hPa to account for tropopause effects. For both domains, the three-dimensional turbulent kinetic energy subgrid mixing scheme that is self-adaptive to the grid size between the large-eddy simulation and mesoscale scales is utilized (Zhang *et al.*, 2018). A revised Monin–Obukhov scheme is used to simulate the surface layer (Jimenez *et al.*, 2012). Additionally, the Noah-MP land-surface model (Niu *et al.*, 2011), the Rapid Radiative Transfer Model long-wave scheme (Mlawer *et al.*, 1997), and the Dudhia short-wave scheme (Dudhia *et al.*, 1989) are used. As discussed in the Introduction, the WDM6 microphysics scheme (Lim & Hong, 2010) is used in D2, while the Kain–Fritsch cumulus parametrization scheme (Kain & Fritsch, 1993) is used in D1.

The WRF domain setup is displayed in Figure 1. The inner domain (D2) encompasses the region covered by the 17 operational radar stations of DWD almost completely. The simulation is performed for the entire month of July 2023, with a temporal output of 5 minutes to provide direct comparison with the 5-minute output of DWD radar data (see below). On average, July has been shown to be the most convectively active month over Germany

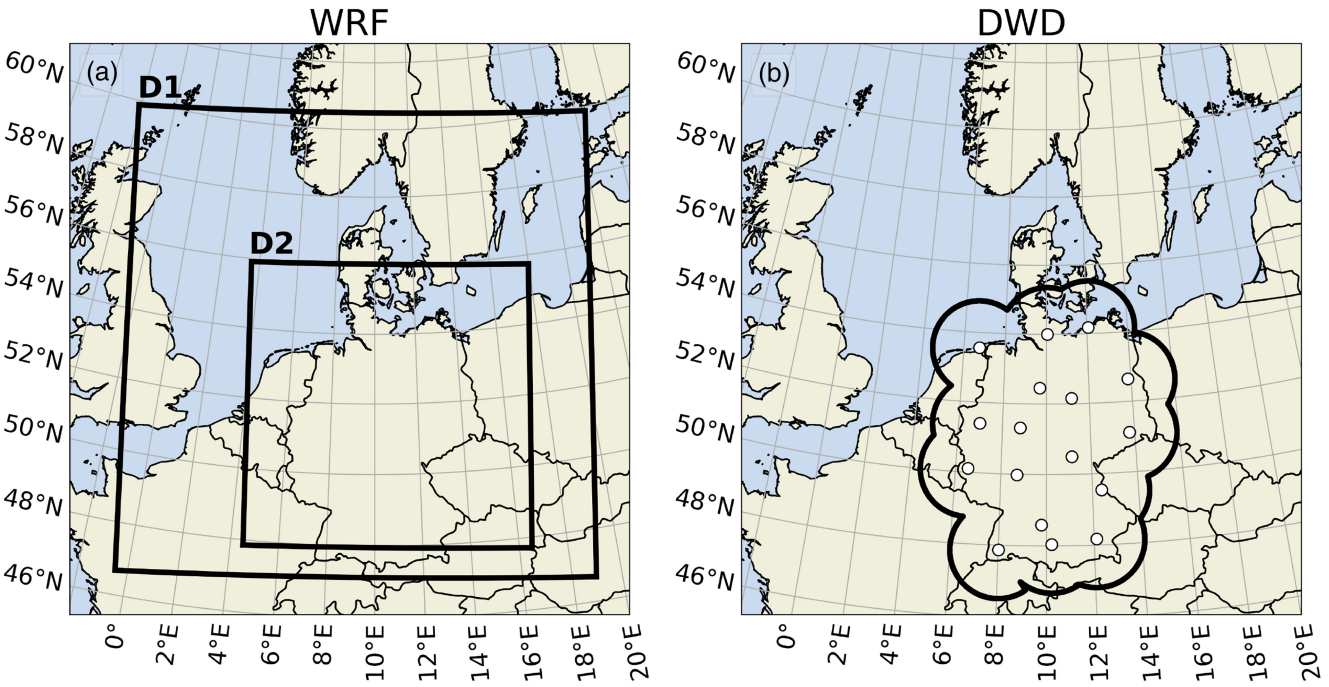


**FIGURE 1** (a) Domain setup for the WRF simulation and (b) maximum area covered by the 17 operational C-band radar stations of the DWD radar network. The locations of the radar stations are shown by white dots. [Colour figure can be viewed at wileyonlinelibrary.com]

(Kirsch *et al.*, 2021; Pacey *et al.*, 2021). The model is initiated at 0000 UTC on July 1, so that the spin-up period (~6 hours) of the model occurs during the night-time, when there are typically very few convective cold pools (see fig. 1c of Kirsch *et al.*, 2021).

The usage of 1-km grid spacing in the inner domain is sufficient for simulating cold pools in terms of their bulk characteristics, such as magnitude, depth, geometric shape, and areal coverage (Squitteri & Gallas, 2020). In general, 1-km resolution is widely considered to be "convection-permitting" (e.g., Wilhelmson *et al.*, 2001), and is used routinely in high-resolution regional modelling. Pryor *et al.* (2023) employed 1.33-km horizontal grid spacing in WRF simulations of deep convection over the southern US Great Plains, and Wagner *et al.* (2018a) showed that 1- or 5-km grid spacing simulations with WRF reproduce the diurnal cycle and spatial structure of precipitation over Germany when compared with radar and station data. Prein *et al.* (2021) noted only modest improvements in mesoscale convective system simulations when grid spacing was reduced below 4 km, while Squitieri and Gallus (2020) found that the statistical properties of cold pools in simulations with 0.333-km grid spacing were similar to those in simulations with 1-km grid spacing, suggesting diminishing returns in forecast fidelity below 1 km. Additional guidance for the choice of grid spacing chosen here was provided by the observational work of Wapler (2021) and Wilhelm *et al.* (2023), who characterized deep convection over Germany using DWD radar data. They showed that only the shortest-lived cells have a cell size of about $\sim 20\ km^2$, and then only during their early and decay stages. This cell size is at the limit of being marginally resolved with 1-km grid spacing (assuming 4–6 grid points are required to resolve a given convective feature). The majority of convective cells, particularly around their peak stage, are considerably larger and should be adequately captured. Moreover, cold pools themselves tend to spread horizontally beyond the initiating precipitation core, increasing their effective spatial scale and making them more amenable to a grid spacing of 1 km. However, finer-scale simulations of 100-m horizontal resolution are recommended in order to capture the turbulent flow associated with cold pools (Fievet *et al.*, 2023; Grant & van den Heever, 2016; Straka *et al.*, 1993). Hirt *et al.* (2020) showed that cold pools are more frequent, smaller, and less intense in lower-resolution simulations using ICON-LES. Furthermore, their gust fronts are weaker and less likely to trigger new convection. Bryan *et al.* (2003) showed that 1-km resolution may be insufficient to reproduce realistic squall-line evolution in idealized settings, due to a lack of resolved turbulence. Given that the focus in this study is not on the finer-scale turbulent features of cold pools, but rather on bulk convective statistics over a large region for a relatively long time period (month-scale), the usage of a 1-km grid spacing is deemed sufficient.

## 2.2 | DWD observational data

The German C-band weather radar network conducts a 5-min interval terrain-following near-surface scan at each of its 17 operational stations (Wapler, 2021; Wilhelm *et al.*, 2023). These scans have a range resolution of 1 km and an azimuth resolution of 1 degree. At radar sites, measurements are taken close to the surface; however, the measurement height increases with distance from the radar due to variations in topography and the effects of atmospheric conditions on radiation propagation. The individual radar sweeps are combined into a reflectivity composite with a horizontal resolution of 1 km, covering Germany and some adjacent regions.

In this study, we utilize both the WN and RV radar composite datasets of the DWD. These composites supply the quality-assured reflectivity and terrain-following near-surface precipitation observations, respectively, over Germany with a resolution of 1 km × 1 km (totalling 1200 × 1100 pixels). The temporal resolution is 5 minutes, and data for the entire month of July 2023 have been analysed in order to provide a direct comparison of radar reflectivity and radar-derived rain rate with the 1-km WRF simulation described above. The extent of coverage by the DWD network is shown in Figure 1.

## 2.3 | TATHU tracking algorithm and convection detection

A new method to track convective systems systematically has been recently developed. The Tracking and Analysis of Thunderstorms (TATHU) toolset allows for the detection, tracking, and analysing of thunderstorm life cycles (Uba *et al.*, 2022; Sena *et al.*, 2024). Originally developed to detect and track thunderstorms in satellite data by utilizing a brightness temperature threshold and overlapping area technique, we have extended the code to process DWD observational radar data and WRF output. Convective elements can be identified via a chosen threshold within a given two-dimensional (2D) field from which TATHU generates a corresponding bounded polygon with a weighted centroid position. Given the polygon boundary at each time step and a user-provided polygon overlap area percentage, the convective elements identified can be tracked in time. Convective element characteristics (centroid position, shape, size) are provided at each time step and statistics (e.g., mean, maximum, minimum, median values) of

the given 2D field related to each convective element can be obtained.

In this study, we define a convective cell numerically as a contiguous area of at least 15 $km^2$ with a minimum radar reflectivity of 19 dBZ. While the size threshold is identical to that used in the DWD detection and nowcasting tool KONRAD, the reflectivity threshold of 19 dBZ is much lower than the 46 dBZ used in recent studies (Wapler, 2021; Wilhelm *et al.*, 2023). The choice of a lower threshold here allows us to track the earlier development phase and later decay phases of deep convective cells in order to capture the cell life cycle more fully. However, due to the 5-minute temporal resolution of the observational data, our chosen thresholds may not capture the very early development, where cells can develop very quickly. Cells that do not attain a value of at least 46 dBZ somewhere within the identified cell are not considered in either the simulation or observational data for the comparisons in Sections 3 and 4, while this threshold must be met at some point during a cell's lifetime to be considered in the life-cycle analysis in Section 5. This means that, for life cycles analysed in Section 5, we should capture development and decay phases. In other studies, a minimum 40-dBZ threshold was proposed (Steiner *et al.*, 1995; Goudenhoofdt & Delobbe, 2013) to identify convective precipitation. Goudenhoofdt and Delobbe (2013) suggest that using lower thresholds can lead to undesirable behaviour in the tracking algorithm employed, with more risk of storms being classified as splitting or merging due to close proximity with other storms. In this regard, TATHU can identify whether storms undergo splitting or merging during their life cycle. However, in the interests of simplicity, thunderstorms that undergo splitting or merging will not be considered in the analysis of Section 5, where life cycles over Germany are investigated in both simulation and observational data. In our analysis, a polygon overlap criterion of 10% is used to connect convective element snapshots over time.

The identification of cold pools has long been a difficult task, even in numerical simulations (Drager & van den Heever, 2017). Typically, in ground-based observational data, cold pools and associated gust fronts can be identified through a sudden drop in temperature and increase in wind speed, often with a provision that some rainfall is detected shortly thereafter (Hoeller *et al.*, 2024; Kruse *et al.*, 2022). In numerical models, a two-dimensional object can be identified at a given height for a variety of different meteorological fields. Drager and van den Heever (2017) and Hirt *et al.* (2020) use a density potential temperature[1] perturbation and rainfall threshold to identify cold pools. Drager and van den Heever (2017) avoid explicitly using a buoyancy threshold for defining cold-pool edges by using the zero contour of the second radial derivative of density potential temperature. Hirt *et al.* (2020) noted that the gust front itself tends to lie just outside the identified cold pools when identified via thermodynamical methods, and therefore they define a cold-pool boundary region as a zone around each cold pool with 25 km width, which is the region most likely to contain the gust front. Fournier and Haerter (2019) also suggest that a thermodynamic approach is lacking and capture of the gust front is unlikely, especially later in cold-pool lifetimes, as turbulent mixing with environmental air weakens temperature gradients at the cold-pool edges. Rather than increase the zone around the identified cold pool by an arbitrary size, they suggest a dynamical cold-pool outflow approach, where the cold-pool edges are based on the minimum in a radial derivative of the wind field from each convective cell. Problems remain, however, in using more realistic simulations, including a complex background flow for associating a given cold pool with a specific parent cell. This is a non-trivial task, as gust fronts of neighbouring cells tend to merge or collide, and calculating radial derivatives emanating from each convective cell centroid for each time step over a large domain is quite computationally expensive.

In this study, for simplicity, the properties of cold pools and associated gust fronts are identified by increasing the size of the thunderstorm polygon by 20% and using the TATHU framework to extract gust-front properties from this larger polygon. This approach, while somewhat similar to Hirt *et al.* (2020), has the potential falsely to include information from neighbouring convective cells, should the increased-size polygon boundaries of two or more cells overlap. There is also the possibility that the strongest wind perturbations are not captured by the increased-size polygon, as the gust front from stronger or older cells may have spread out to larger distances. A more rigorous definition of cold-pool detection and association with the parent cell is the topic of future work.

## 3 | CONVECTIVE SNAPSHOT CHARACTERISTICS

In this section, a comparison is offered between the convective characteristics in the simulation and the observational dataset from DWD. Snapshots of convection are produced at every 5-minute output for the month of July 2023 in both the WRF simulation (D2) and the entire DWD radar observation network. Individual convective cells are considered in the characteristics, provided that the minimum threshold of 46 dBZ is attained somewhere within the cell at each snapshot. By considering independent snapshots in this way, it is apparent that any given individual cell will likely be counted multiple times during its life

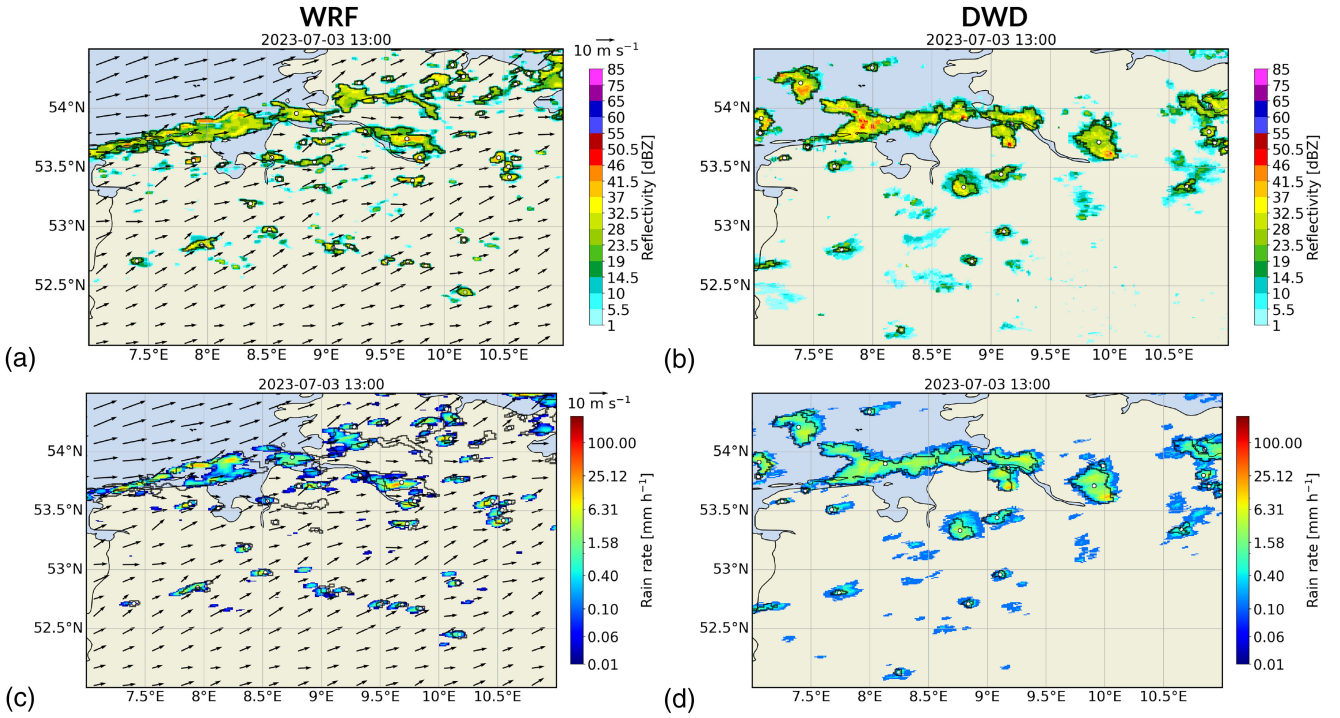


**FIGURE 2** Horizontal cross-sections of radar reflectivity in (a) WRF at a height of 1 km and (b) the DWD WN dataset; rainfall rate in (c) the WRF simulation and (d) the DWD RV dataset. Shown is a snapshot on July 3, 2023, 1300 UTC, with a focus over northern Germany. Wind vectors ($m \cdot s^{-1}$) at a height of 10 m are shown in the WRF simulation (left panels), with the reference vector given in the upper right of each panel. Radar reflectivity (dBZ) and rainfall rate ($mm \cdot h^{-1}$) are given in the colour bars on the right of each panel. White dots identify the polygon centroids for identified cells, while black contours indicate polygon outlines for cells that meet the thresholds defined in Section 2.

cycle in this analysis. In this section, we also do not distinguish whether a cell has undergone a merge or split event. Life cycles and a Lagrangian perspective of simple isolated cell evolution are discussed in Section 5. It must also be considered that the domain size is not completely identical in the simulation and in the observational network, so the total number of convective cells identified would not be expected to be the same. However, the focus in this section is on the ability of WRF to capture the bulk convection characteristics (e.g., radar reflectivity, derived rain rate, cell morphology) found in observations.

Figure 2 shows a snapshot of the convective situation on July 3, 2023 at 1300 UTC, with a focus over northern Germany. The reflectivity (top) and rainfall rate (bottom) are shown in the WRF simulation and DWD radar observations. This day in particular was very convectively active over northern Germany. The ability of the TATHU algorithm to detect convective features is demonstrated, with contours enveloping convective elements that meet the threshold requirements. At this time, it can be seen that, while there is not a complete agreement in the location of each individual cell, the WRF simulation broadly captures the convective situation. A complete agreement at any given time would not be expected, due to the stochastic nature of convective initiation. Cells that meet the threshold of 19 dBZ (with a minimum area of 15 $km^2$) and are detected by the TATHU algorithm are encircled by a black contour (upper panels, blue contour in lower panels). The lower panels show that the regions of maximum rainfall rate occur within the polygon defined by the reflectivity threshold. Figure 3 shows similar snapshots comparing the simulation and observations at different times throughout July 2023, but covering a larger region. Furthermore, Figure 3g shows convective cell count per day in both simulation and observations for the 30-day period investigated. This figure indicates that the simulation captures the overall trends and variability in convective activity well, supporting the idea that WRF can reproduce the bulk statistical and structural characteristics of convective systems over extended periods, even at 1-km resolution. WRF captures periods of reduced (Figure 3c,d) and enhanced convective activity (Figure 3e,f) reasonably more than halfway through the 30-day simulation.

Statistics for each individual convective snapshot, at each 5-minute output for the whole month, are presented in Figure 4. Shown are histograms of the mean reflectivity, maximum rainfall rate, size, and geometric shape within each polygon detected (87,904 snapshots for WRF,

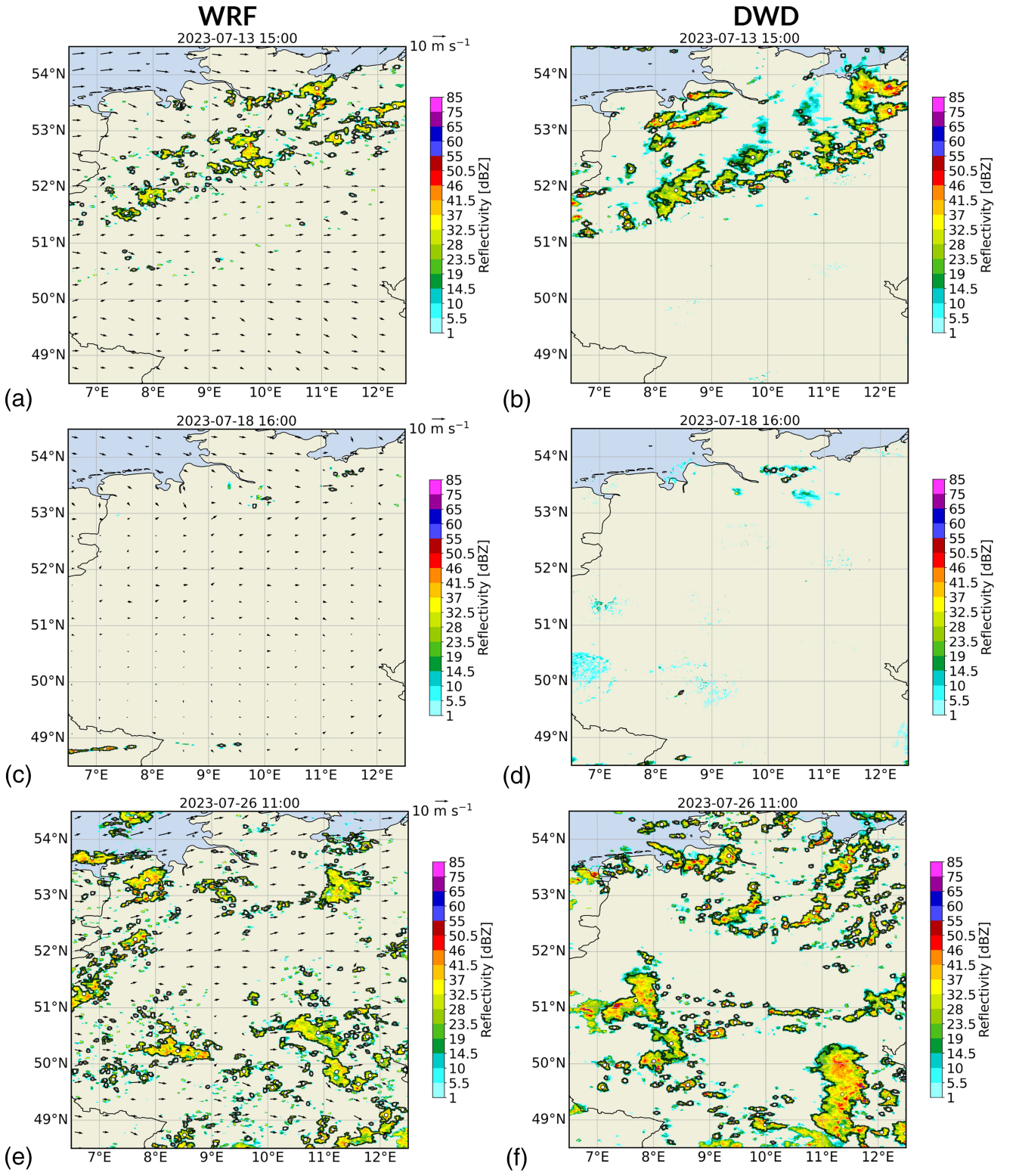


**FIGURE 3** Horizontal cross-sections (a)–(f) as in Figure 2, but covering a larger region of the model domain and radar network at various times. Panel (g) shows convective cell count per day, as identified by the TATHU algorithm as per the defined thresholds, in the WRF simulation for the entire WRF domain D2 and for the whole DWD radar network.

93,430 snapshots for observations). The distribution for the mean reflectivity within a given cell is relatively similar in both WRF and the observations (Figure 4a,b), with a clear Gaussian distribution and relatively small skewness factor. The mean and median are slightly higher in WRF, however (the WRF mean and median are 32.24

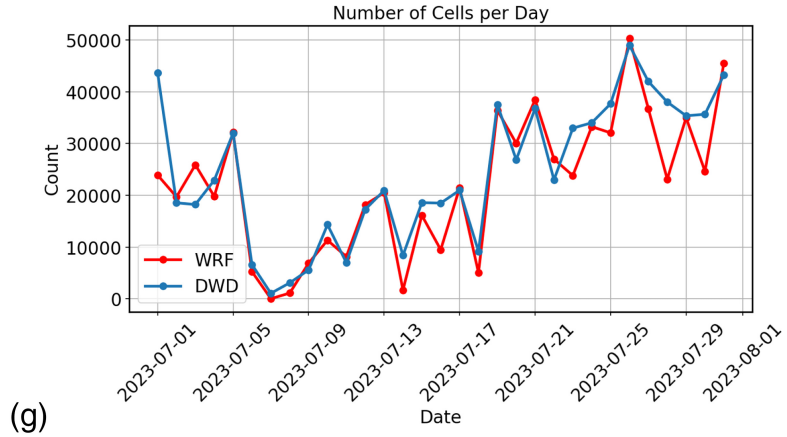


**FIGURE 3** (Continued)

and 32.15 dBZ, respectively, compared with 31.43 and 31.18 dBZ in observations). The kurtosis value is close to zero for both, suggesting both distributions have moderate tails and a bell-shaped curve. The rain-rate distribution is not as comparable (Figure 4c,d), with a notable positive bias of high maximum rain rate in WRF (median of 31.83 mm $\cdot$ h$^{-1}$ in WRF, compared with 23.28 mm $\cdot$ h$^{-1}$ in observations), a result that has previously been found in the model (Pryor *et al.*, 2023). The kurtosis value here highlights the tendency for heavier tails and a sharper peak, meaning more of the variance is from infrequent extreme deviations. WRF also tends to produce smaller convective cells than in observations (Figure 4e,f), with a median size of 121.09 km$^2$ compared with 225.65 km$^2$ in observations. Extreme values in the tails are common for cell size distribution (as seen in both kurtosis and the standard deviation), as larger mesoscale convective systems tend to occur much less often in nature compared with the more frequent small-scale popcorn-like convection. Despite the bias towards smaller cells, the convective cell shape, as shown by the ellipsoid ratio (Figure 4e,f), is almost identical. Observed deep convection over Germany is typically elliptical in shape, with a median ratio of the major to minor axis of 1.62. In WRF, the median elliptical ratio (1.52) is very close to observations, indicating that WRF is capturing the background flow reasonably well, which plays a role in the stretching of cells into an elliptical shape (Parker, 1996). These values are also very close to those found in observations by Kirsch *et al.* (2024), who showed that cold pools themselves have aspect ratios between 1.5 and 1.6. While the average cell is rather elongated, the situation at any given time can represent more isolated circular cells and highly elongated systems, as shown in Figure 2, which demonstrates the variability in convective geometric shape at a given time. The shape of isolated convective cells throughout the convective life cycle is discussed in Section 5.

In order to quantify the comparisons shown in Figure 4, we implement a statistical method, which is useful for measuring the similarity between two probability distributions with different sample sizes. The so-called *Jensen–Shannon divergence* (JSD) metric (Schütze & Manning, 1999) is valid for comparing any shape of probability distribution, including non-Gaussian distributions. If the JSD is zero, the two distributions being compared are identical, while if it is close to 1 then the two distributions essentially do not overlap at all. Values of JSD $< 0.1$ suggest that the two distributions are very similar, while values of up to 0.5 indicate some degree of overlap. For the distributions presented in Figure 4, we find corresponding JSD values of 0.130, 0.170, 0.185, and 0.059 for mean reflectivity, maximum rain rate, convective area, and ellipsoid ratio, respectively. WRF captures the distribution of mean reflectivity reasonably well (JSD = 0.130), but does not capture the maximum rain rate as well (JSD = 0.170). While the model does extremely well at capturing observed convective cell shape (JSD = 0.059), the distribution of cell size is the least well-captured quantity shown here (JSD = 0.185).

Figure 5 shows the properties of convective cell propagation direction and propagation speed in both WRF and observations for any convective cell that can be connected consecutively in time with the TATHU algorithm using the previously defined overlap criteria (i.e., in this case for at least two consecutive time steps). These quantities are calculated from the difference in the ellipsoid centroid between two consecutive time steps for each cell. Convective cell propagation direction (Figure 5a,b) is close to identical, with a difference of about 1° between simulation and observations, indicating that WRF is capturing the large-scale background flow direction reasonably well throughout the period investigated. The JSD score for these two distributions is 0.027, which suggests that they are almost identical. WRF has previously been shown to reproduce mesoscale flow features accurately

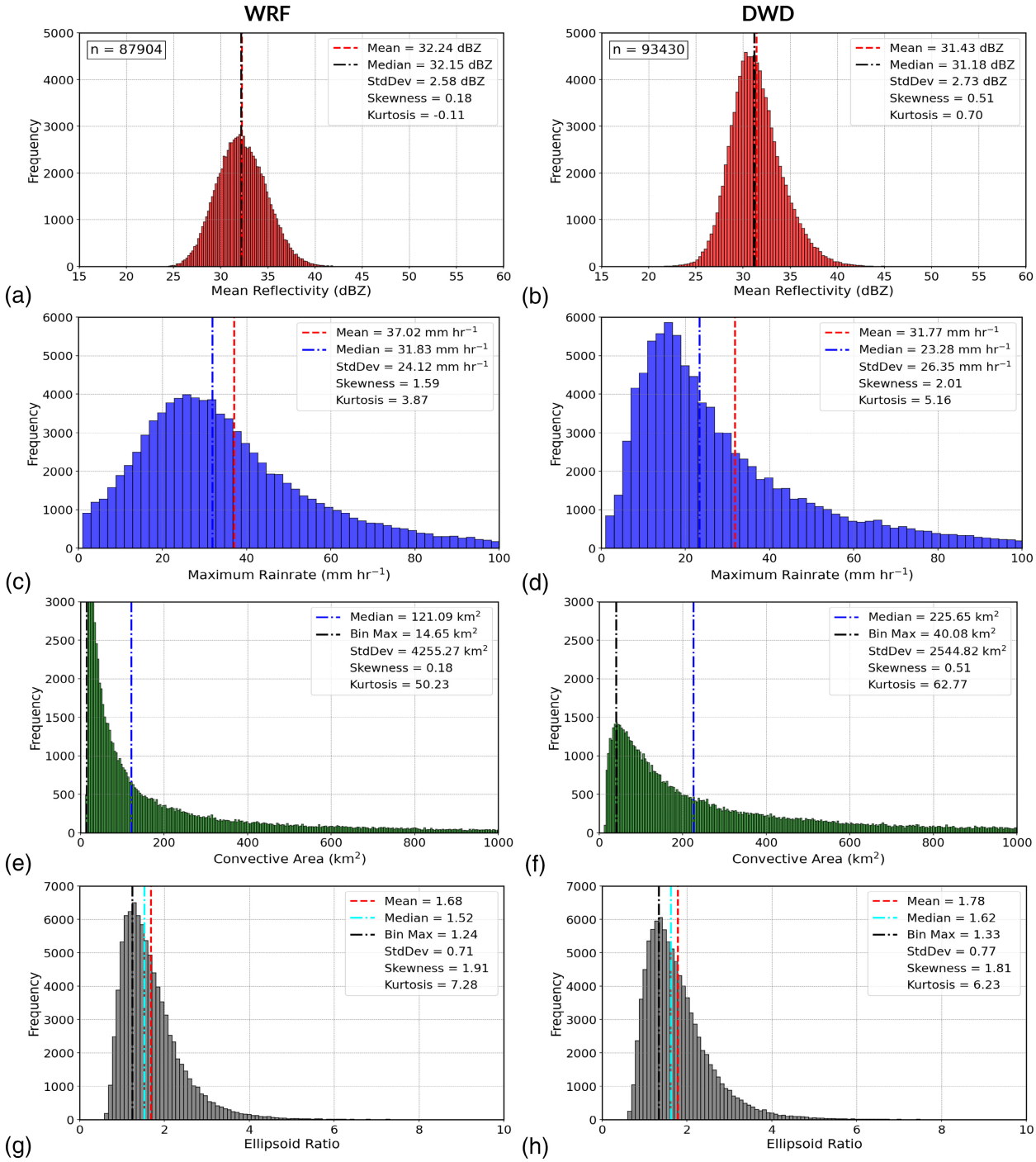


**FIGURE 4** Histograms of (a,b) mean radar reflectivity (dBZ), (c,d) maximum rainfall rate (mm · h$^{-1}$), (e,f) convective area (km$^2$), and (g,h) ellipse ratio for each individual cell snapshot detected in the WRF simulation (left panels) and the DWD observations (right panels) that exceeds the thresholds defined in Section 2. Vertical lines show the mean, median, or bin maximum value, according to the label bar in each panel. Sample size is given in the top panels.

over long time periods (month-scale), even over complex terrain (Wagner *et al.*, 2018b). Here, convective cells typically propagate from the west–southwesterly direction, and it is extremely rare (at least during the month analysed) for cells to propagate from an easterly direction. The median cell propagates slightly faster in observations by 0.77 m · s$^{-1}$; however, the distribution of propagation speeds is captured very well (JSD = 0.070). Overall, this result indicates that WRF is capturing the large-scale bulk shear magnitude and direction well (isolated, non-supercellular convection is typically advected along with the background flow: Cotton *et al.*, 2010).

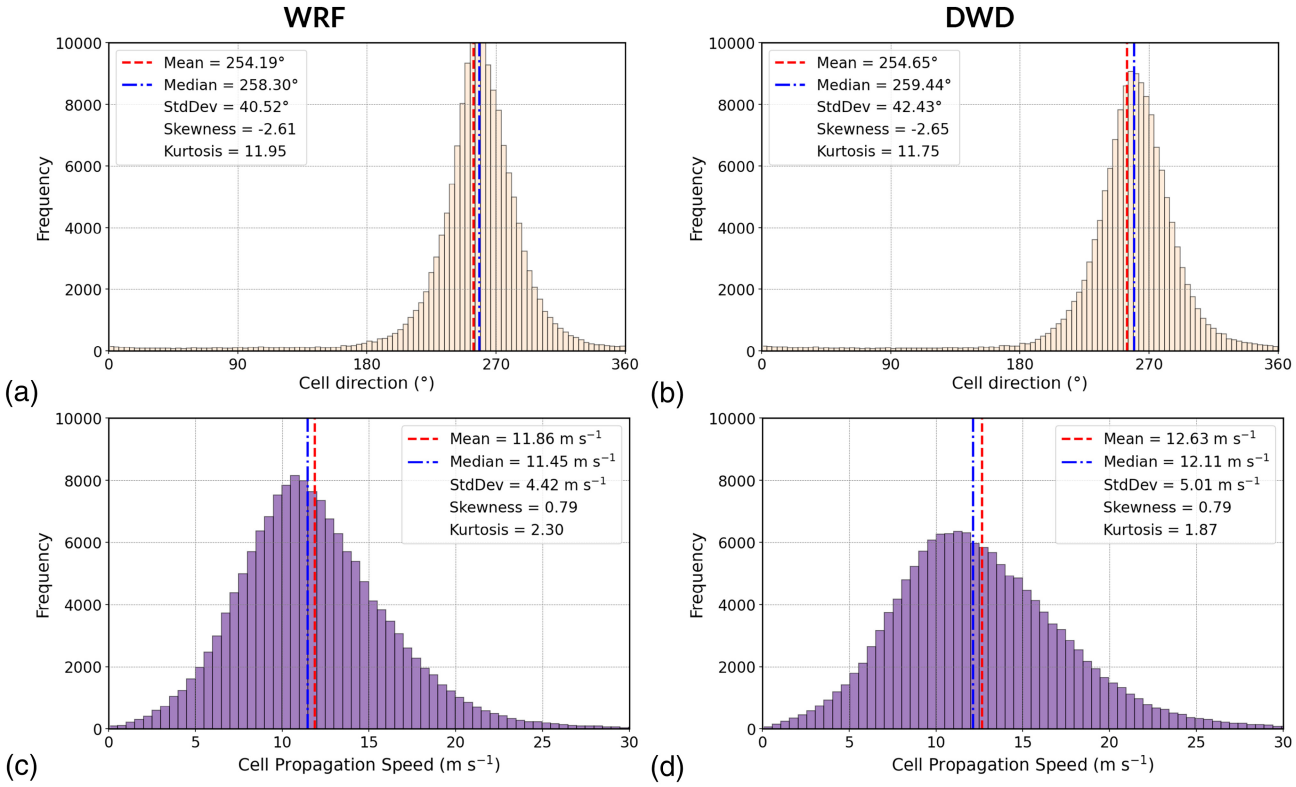


**FIGURE 5** Histogram of convective cell propagation direction (°, top panels) and propagation speed (m · s$^{-1}$, bottom panels) in WRF (left panels) and DWD observational data (right panels). Vertical lines show the location of the mean and median value, according to the label bar in each panel.

In summary, WRF captures the distribution of convection over Germany well for the month of July 2023. Despite the bias towards smaller cells that rain at a higher rate than observed, the mean radar reflectivity and convective shape are captured well. Cell propagation direction is captured particularly well, although the speed at which cells propagate is underestimated slightly. Although the convective shape and propagation direction are captured well by WRF, these features are not directly related to the cold pools, but rather to the parent cell that generates the cold pool. In the next section, we investigate additional characteristics of deep convection, including those for cold pools, with a particular focus on quantities relevant to wind energy.

## 4 | CONVECTION AND COLD-POOL CHARACTERISTICS RELEVANT TO WIND ENERGY

An aim of this work is to quantify the potential impacts of convective cold pools for wind-energy applications. In the previous section, we evaluated the model against available observations in order to determine whether WRF can capture bulk characteristics (reflectivity, rain rate, and morphology) of convection over Germany. In this section, we begin to analyse additional model output relevant to wind energy, including wind speeds and temperature changes. One particularly important aspect is to quantify how much the temperature changes during convective cold-pool passages. When a cold pool traverses a wind turbine, the temporary stabilization of the boundary layer affects the strength and duration of the turbine-induced turbulent wake, with stable conditions leading to lower turbulence and thus longer-lasting wakes (Englberger & Doernbrack, 2018). Longer-lasting wakes are more relevant, for example, over wind parks, where additional turbines downwind can also be affected. Another important aspect is the sudden increase in wind speed and the associated change in rotor-layer vertical shear, which can stress turbine blades (Kelly *et al.*, 2021). These increased loads not only accelerate wear and tear but also heighten the risk of mechanical failure.

In an effort to identify and quantify cold-pool characteristics conservatively using enlarged polygons (see Section 2.3), we limit the subsequent analyses to convective cells which (1) contain a reflectivity value of at least 46 dBZ for a given time step, to focus on convective precipitation, and (2) attain a minimum 2-m virtual potential temperature ($\theta_v$) difference of at least −1.5 K

at some grid point within the enlarged polygon, similar to observed temperature detection thresholds used for cold-pool studies over Europe (Kirsch *et al.*, 2021; Kruse *et al.*, 2022). From this subset of convective snapshots, we show histograms of various quantities for each individual cell detected in the WRF simulation (Figure 6). Quantities are expressed as a mean, where the given variable is averaged over the whole cell polygon, or a minimum or maximum, which is a point value within the cell. The minimum 2-m $\theta_v$ difference and the maximum 10-m wind-speed perturbation are obtained by subtracting a given field from a two-hour rolling mean. The stability and shear exponent $\alpha$ are calculated over heights from 60 to 160 m, which we refer to as the rotor-layer region. In atmospheric boundary-layer studies, the wind-shear exponent ($\alpha$) is a dimensionless parameter that characterizes the vertical variation of wind speed with height. It is commonly derived from the power-law equation:

$$U(z) = U_{\text{ref}}\left(\frac{z}{z_{\text{ref}}}\right)^{\alpha}, \tag{1}$$

where $U(z)$ is the wind speed at height $z$, $U_{\text{ref}}$ is the wind speed at a reference height $z_{\text{ref}}$, and $\alpha$ is the wind-shear exponent, which depends on surface roughness and atmospheric stability. For the height range 60–160 m, $\alpha$ provides insight into the change in wind speed within the lower part of the atmospheric boundary layer.

The cold-pool intensity is calculated as in Benjamin (1968) and is an integral of the negative buoyancy from the surface to the cold-pool depth, which is defined as the height above the surface where the buoyancy goes from negative to zero. Cold-pool intensity is given as

$$CI^2 = -2\int_0^H B\, dz, \tag{2}$$

where $B$ is the buoyancy, $z$ is the height, and $H$ is the depth of the cold pool.

The additional filter (a 2-m $\theta_v$ difference of at least −1.5 K at some grid point within the cell polygon boundary) removes nearly 30,000 cell snapshots from the analysis (compared with Figure 4), suggesting that implementing a threshold of 46 dBZ leads to the inclusion of about one-third of cells that do not have a distinct convective cold pool from the background environment. The minimum $\theta_v$ difference identified here is found within the cell polygon boundary and not out ahead of the cell, where the gust front is often located. We justify this decision based on the results of Kirsch *et al.* (2024), who showed that the median temperature perturbation is generally strongest at the centre of the cold pool and decreases linearly in strength towards the gust-front edge. For the wind-speed perturbation, it is pertinent to search outside the cell boundary, and an approach similar to Hirt *et al.* (2020) is implemented where the search area is increased. The maximum 10-m wind speed for a given cell is found within a polygon, centred on the original cell polygon centroid but increased by 20% of its original size. The method used expands the polygon shape uniformly in all directions, while preserving the shape of the original polygon.

For the simulated month, the median minimum 2-m $\theta_v$ difference is −2.95 K (Figure 6a), which compares well with values found in observational studies (Kirsch *et al.*, 2021, 2024; Kruse *et al.*, 2022). In particular, extreme cases tend to level out at around −10 K (Figure 6a), similar to the extreme values found in observations (−10.8 K) by Kirsch *et al.* (2021). In almost every snapshot, the cold pool is accompanied with a stable environment, as indicated by the mean $\theta_v$ stratification in the cell, calculated from 60 to 160-m height. The median stability in a simulated cold-pool environment is 2.9 $\text{K} \cdot \text{km}^{-1}$. The maximum 10-m wind speeds within the cell are shown in Figure 6c and the maximum perturbations to the time-averaged background flow are shown in Figure 6d. Median wind-speed perturbations (4.28 $\text{m} \cdot \text{s}^{-1}$) match those found in observations very closely (4.4 $\text{m} \cdot \text{s}^{-1}$ in Kruse *et al.*, 2021). Extreme values of over 10 $\text{m} \cdot \text{s}^{-1}$ can occur, but are relatively rare.

Typically, also associated with cold pools is an increase in vertical shear over the rotor layer, due to the protruding nose-like structure of cold-pool gust fronts, with maximum winds occurring close to 100-m height. Observed mean values of shear exponent $\alpha$ have been found in northern Germany and Denmark to be typically of the order of 0.25–0.3 (Kelly *et al.*, 2014; Wildmann *et al.*, 2022). In the WRF simulation, the median is slightly larger than observed, while the mean is almost double that (Figure 6e). This implies particularly large values of shear in the tail of the distribution, and these large values are presumably associated with the strongest cold pools. A more detailed analysis of cold-pool-associated vertical shear in the WRF model, including its vertical structure and an evaluation with available ground-based observations, is the subject of a future study.

Cold-pool depth and intensity (Figure 6g,h) are nearly normally distributed, with a median cold-pool intensity of 9.06 $\text{m} \cdot \text{s}^{-1}$ and a depth of 2.2 km. These values are somewhat lower than those found in a study of simulated squall-line cold pools, also using the WRF model with 1-km grid spacing (Fan *et al.*, 2017). The median cell averaged 2-m saturation deficit is 3.78 $\text{g} \cdot \text{kg}^{-1}$ (Figure 6f). Cold pools tend to be stronger when the near-surface saturation deficit is larger, as this allows for increased evaporation of rainfall, leading to increased evaporative cooling. Kirsch *et al.* (2021) found a median value of 4.7 $\text{g} \cdot \text{kg}^{-1}$ in cold

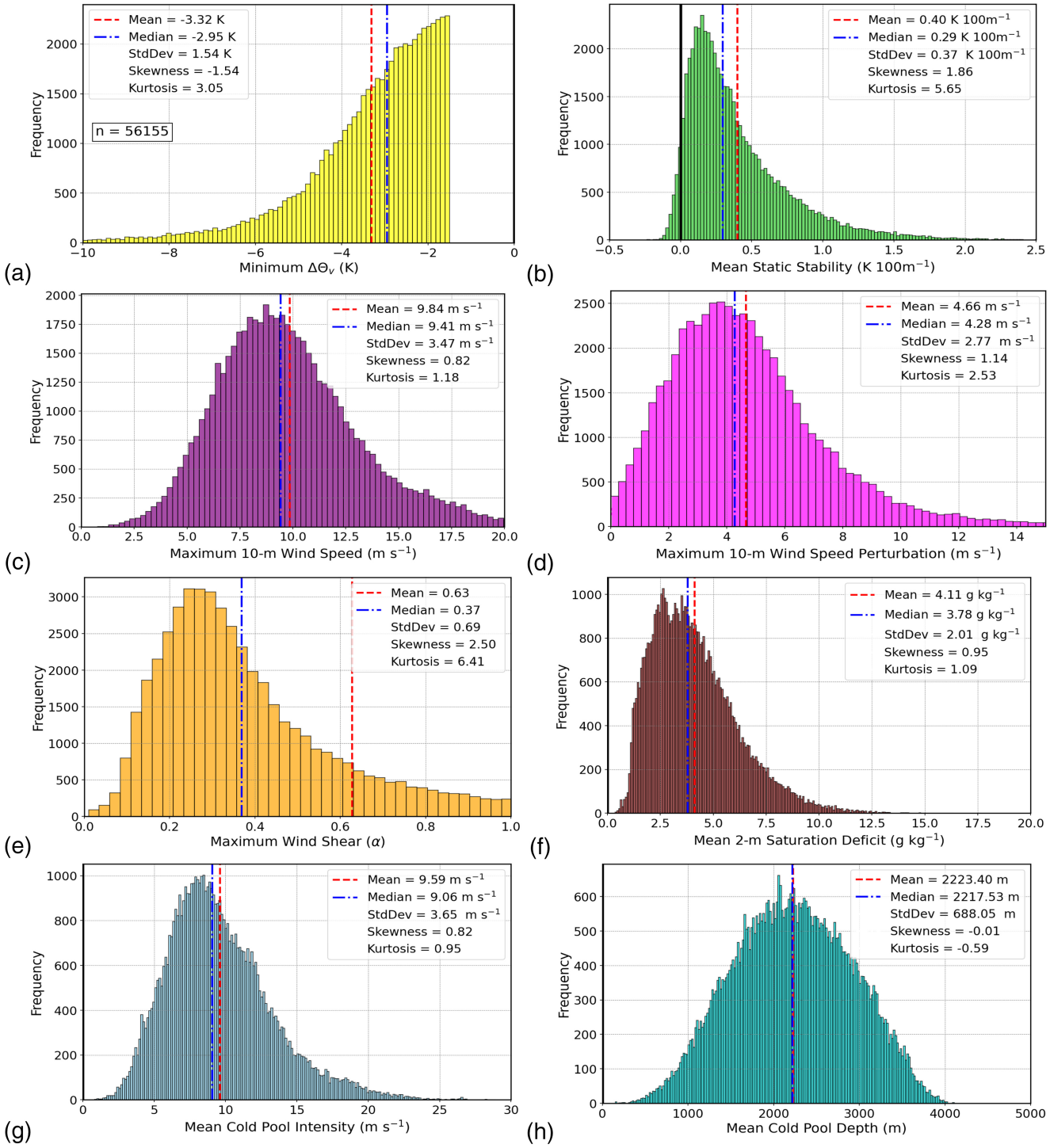


**FIGURE 6** Histograms of (a) minimum 2-m $\theta_v$ difference (K), (b) mean stability (K · (100 m)$^{-1}$), (c) maximum 10-m wind speed (m · s$^{-1}$) and (d) maximum 10-m wind-speed perturbation from a two-hour rolling mean (m · s$^{-1}$), (e) maximum wind-shear exponent alpha over the rotor layer, (f) mean 2-m saturation deficit ($q_{sat} - q$, g · kg$^{-1}$), (g) cold-pool intensity (m · s$^{-1}$), and (h) cold-pool depth (m) for each individual cell snapshot detected in the WRF simulation, where the cell attains the minimum thresholds defined in Section 2. Vertical lines show the location of the mean and median value, according to the label bar in each panel.

pools during the summer months near Hamburg, and they also showed a relatively strong inverse relationship of near-surface temperature perturbation with pre-event saturation deficit.

In summary, the parent convective cell and cold-pool characteristics in WRF are close to observed median values for all available variables. The observed median and extreme minimum 2-m $\theta_v$ differences are captured

well. The median wind gust strength is also very close to the few observations available (4.28 $m \cdot s^{-1}$ compared with observations of 4.4 $m \cdot s^{-1}$), and the modelled results show that extreme 10-m wind-speed perturbations over 10 $m \cdot s^{-1}$ can occur. Presumably, large values of shear exponent $\alpha$ are associated with these extreme cases. The results indicate the possibility of very large stresses on wind turbines from the most intense cold-pool events (Kelly *et al.*, 2021).

## 5 | LIFE-CYCLE CONVECTION AND COLD-POOL CHARACTERISTICS

In this section, we answer the question: How do convective cold-pool characteristics that are relevant for wind-energy applications evolve through a typical convective cell life cycle? This is important to understand, as, from point-source observations, it is often not clear which stage in its lifetime the cell has reached, and therefore it is not clear whether the impact on a turbine could have been stronger. In particular, for nowcasting applications, it is important to quantify the potential impact of a given cell at any point in its lifetime. In the following, convective cells are linked in time using a polygon overlap criterion of 10% using the TATHU framework, and for cells to be considered they must reach the 46 dBZ reflectivity (simulation and observations) and −1.5 K $\theta_v$ difference (simulation only) thresholds at some point in their life cycles. As the focus here is on isolated single-cell convection, cells must not have undergone a splitting or merging event during their life cycle.

In Figure 7, we offer a comparison of simulated and observed life-cycle quantities, previously presented as snapshots in Figure 4, with tracked cells split into two categories: shorter-lived cells (20–60 min) and longer-lived cells (1–2 h). The split into two categories of lifetime duration is performed to investigate whether there are any fundamental differences between shorter- and longer-lived convective cells. The number of trackable cells is dramatically lower than the number of snapshots analysed in the previous section, and there are approximately 25% fewer cells tracked in time in the WRF output compared with the observations. We show that simulated convective cells tend to peak earlier in intensity and attain a higher maximum intensity (as shown by both mean reflectivity and maximum rain rate; Figure 7a–d) compared with observations. This suggests that, in WRF, convective cells develop too quickly and the very early phases are difficult to capture using the criteria defined in this study. The life-cycle rain rates (Figure 7c,d) confirm the high rain-rate bias in WRF discussed in Section 3. The intensity trend differences are less pronounced for long-lived cells, which peak in intensity roughly 25% of the way through their lifetime.

At all points in the life cycles shown here, the simulated convective cell is raining at a much higher rate than in the observations (Figure 7c,d). One possible explanation for this lies in the choice of horizontal grid spacing. Idealized simulations by Bryan and Morrison (2012) demonstrated that grid resolution affects cloud water evaporation, cold-pool dynamics, and rainfall characteristics significantly. Coarser grid spacing tends to produce deeper clouds and more rainfall due to reduced entrainment, while higher-resolution simulations exhibit greater cloud water evaporation, in part due to the development of resolved turbulence. This implies that, at 1-km grid spacing, there is a risk that simulated cells produce excessive rainfall while simultaneously underestimating evaporative cooling and cold-pool strength. As seen in Section 3, simulated convective cells tend to be smaller in area and with a smaller range of convective areas, but both short- and long-lived simulated cells peak in size halfway through their lifetimes, as in observations (Figure 7e,f). This agrees well with the symmetric upside-down parabola archetype described by Wapler (2021) and Wilhelm *et al.* (2023). A possible reason for the smaller cell sizes in WRF lies in the choice of microphysics scheme, with the WDM6 scheme tending to produce smaller stratiform rain regions surrounding convection (Putnam *et al.*, 2016), which may reduce the overall size of the polygon that our tracking algorithm generates. Convective cell shape is remarkably consistent throughout convective lifetimes regardless of the lifetime duration, being more elongated than circular and with a similar range between simulations and observations (Figure 7g,h).

Figures 8 and 9 extend the life-cycle analysis to convective cold pool (Figure 8) and wind-energy (Figure 9) relevant quantities. Cold-pool strength (shown by the minimum 2-m $\theta_v$ perturbation from a 2-h running mean) reaches a minimum of roughly −2.5 K about 50% through the cell lifetime (Figure 8a), regardless of lifetime duration. This closely follows the lifetime trends for maximum surface wind speed, which peaks at 8 $m \cdot s^{-1}$ (Figure 8c), and cold-pool intensity, which peaks at just over 10 $m \cdot s^{-1}$ (Figure 8e). All of these lifetime trends closely follow that of convective area (Figure 7e). Surface moisture increases over a cell's lifetime as precipitation evaporates within the boundary layer, with more moisture present below longer-lived cells. This manifests as a decrease in time in 2-m saturation deficit (Figure 8b), implying that rain is falling into a more saturated environment with time, and thus there is less cooling produced from evaporation with time (Figure 8a). The maximum surface wind-speed perturbation (used as a proxy for the cold-pool gust front) follows an inverse pattern to the 2-m saturation deficit,

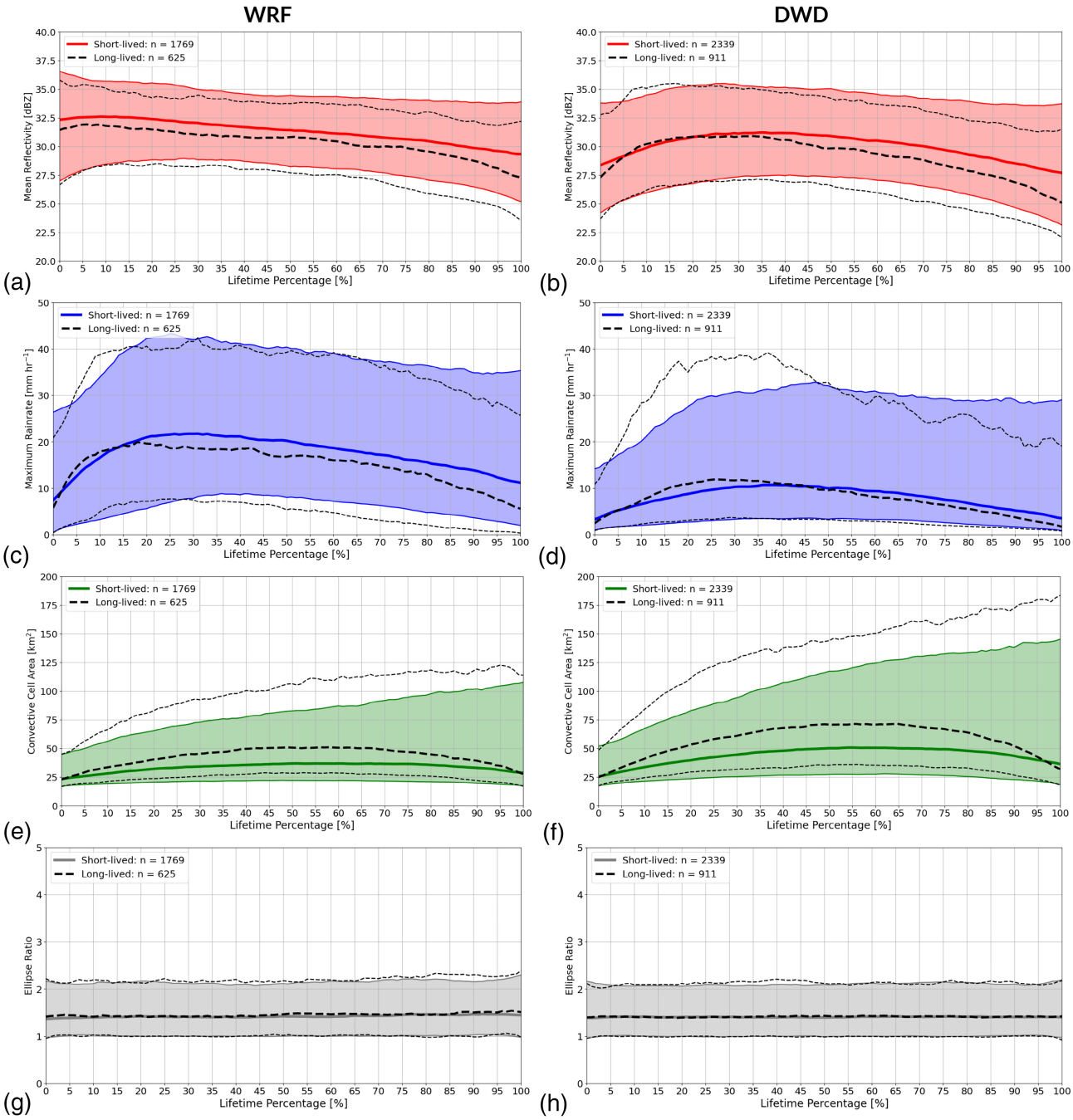


**FIGURE 7** Life-cycle evolution of (a,b) mean radar reflectivity (dBZ), (c,d) maximum rainfall rate (mm · h$^{-1}$), (e,f) cell size (km$^2$), and (g,h) ellipse ratio for the WRF simulation (left panels) and the DWD observations (right panels). Cell life cycles are split into two categories, short-lived cells, which have a cell duration of between 20 and 60 minutes, and long-lived cells with duration of 1–2 hours. The life cycles are normalized by cell lifetime and variables and presented as a percentage of total lifetime. In all panels, the solid coloured curve represents the median of the given variable for the shorter life cycles, while the shaded region encompasses the 10th–90th percentile values. Thick black dashed curves represent the median longer-lived life cycles, and thin black dashed curves encompass the 10th–90th percentiles for longer-lived cells. [Colour figure can be viewed at wileyonlinelibrary.com]

with stronger surface wind anomalies of about 3 m · s$^{-1}$ during the middle portion of the lifetime for longer-lived cells (Figure 8d).

Convective cold-pool depth (Figure 8f) similarly increases during cell lifetimes to roughly 2000 m regardless of lifetime duration, indicating a progressively deeper layer of evaporative cooling. Interestingly, the difference between shorter- and longer-lived storms in terms of cold-pool gust-front strength does not seem to relate strongly to cold-pool depth or temperature perturbation,

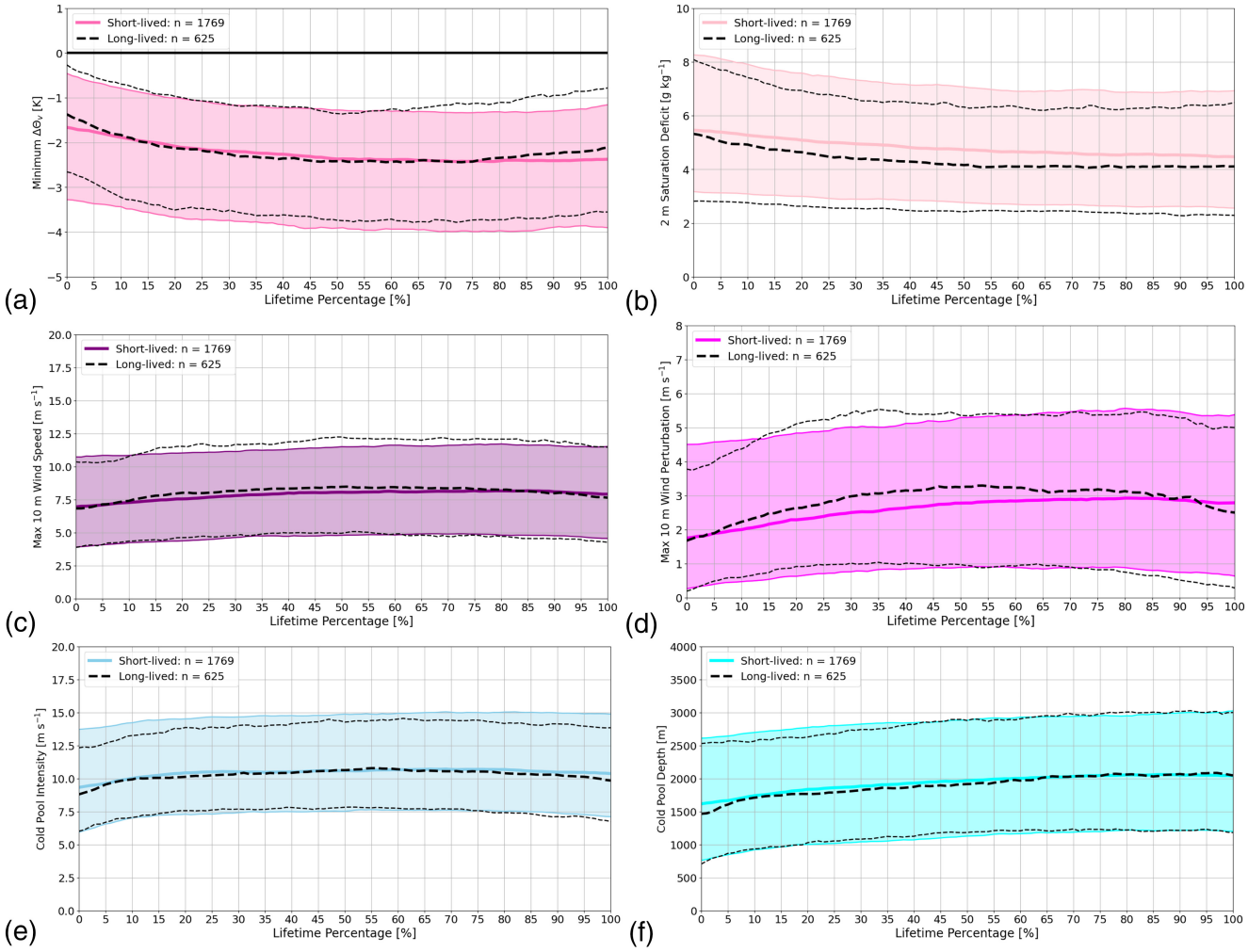


**FIGURE 8** Life-cycle evolution of (a) minimum 2-m $\theta_v$ difference (K), (b) 2-m saturation deficit ($q_{sat} - q$, g · kg$^{-1}$), (c) maximum 10-m wind speed (m · s$^{-1}$), (d) maximum 10-m wind-speed perturbation (m · s$^{-1}$) from a two-hour rolling mean, (e) cold-pool intensity (m · s$^{-1}$), and (f) cold-pool depth (m) for the WRF simulation. Cell life cycles are split into two categories, as in Figure 7. A solid black line shows 0-K temperature difference in panel (a). [Colour figure can be viewed at wileyonlinelibrary.com]

as suggested by density-current theory. Rather, surface wind-speed perturbations more closely follow the trend of convective area. This indicates that a greater volume of evaporative cooling likely present below longer-lived cells influences the cold-pool gust-front strength positively, even more so than convective intensity or surface temperature perturbation. Kirsch *et al.* (2021) observed that evaporative cooling in the subcloud layer is the primary factor controlling cold-pool temperature perturbations, with a stronger correlation with pre-event saturation deficit than accumulated rainfall.

Figure 9a shows the maximum shear exponent $\alpha$ over the typical turbine rotor-layer height (60–160 m). Shear is slightly greater during the middle portion of the cell lifetime. This aligns with the maximum surface wind-speed perturbation, indicating a generally positive relationship between a surface cold-pool gust front and the associated convective-cell rotor-layer shear. Longer-lived cells have slightly higher shear than shorter-lived ones. Rotor-layer static stability (Figure 9b) increases during a cell's lifetime, with longer-lived storms having greater stability around the 50% point in their lifetimes. This would indicate that, the older a cell, the stronger the stabilization of the cell environment that occurs. At the very early stages of cell development, the median static stability is close to zero.

Figure 9c,d shows the mean and maximum 100-m wind speed. This variable is an important quantity for wind-energy applications, as typically the hub height for most turbines is close to 100 m. The 100-m wind speed averaged over the cell does not change considerably through the cell life cycle (Figure 9c). Calculating a mean wind over the cell polygon is equivalent to calculating the background flow through the cell, as perturbations in the cell polygon cancel out through spatial averaging.

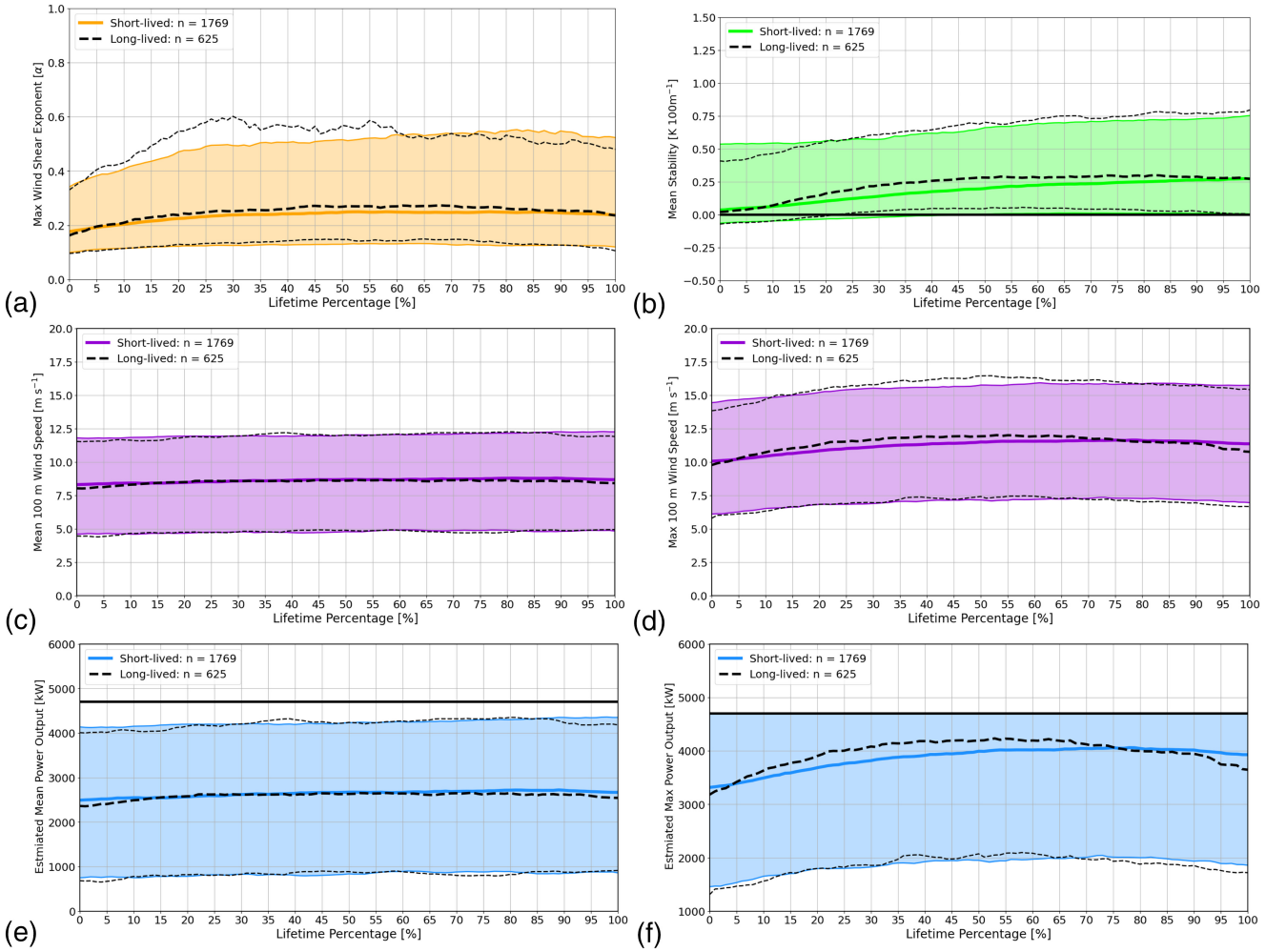


**FIGURE 9** Life-cycle evolution of (a) maximum wind shear over the rotor blade heights (shear exponent $\alpha$), (b) mean rotor blade stability ($K \cdot (100\ m)^{-1}$), (c) mean 100-m wind speed ($m \cdot s^{-1}$), (d) maximum 100-m wind speed ($m \cdot s^{-1}$), (e) mean estimated power output (kW), and (f) maximum estimated power output (kW) for the WRF simulation. Cell life cycles are split into two categories, as in Figure 7. A solid black line highlights the $0\ K \cdot km^{-1}$ threshold in panel (b) and the maximum power output for the standard turbine structure in panels (e,f). [Colour figure can be viewed at wileyonlinelibrary.com]

Figure 9c shows that the median cell does not likely propagate faster as it evolves in time. Pichault *et al.* (2022) also showed that convective cold pools move with the background mean flow from LIDAR observations. In contrast, the maximum 100-m wind speed shows a downward-facing parabolic evolution in time (Figure 9d), similar to the 10-m wind maximum (Figure 8c). For longer-lived cells the median wind speed peaks sooner, close to halfway through the lifetime, whereas it occurs at closer to 75% of the life cycle for shorter-lived cells.

An estimate of power output can be calculated from the hub-height wind speed through a simple piecewise relationship (Wildmann *et al.*, 2022), where the wind speed is applied to a simplified power curve and turbine operational adjustments (e.g., blade pitching, turbine yawing, etc.) are not taken into account. The power output $P$ (in kilowatts) as a function of wind speed $U$ (in $m \cdot s^{-1}$) is given by

$$P(U) = \begin{cases} 0, & U < U_{\mathrm{cut_{in}}} \text{ or } U \geq U_{\mathrm{cut_{out}}}, \\ P_{\max} \cdot \frac{U - U_{\mathrm{cut_{in}}}}{U_{\mathrm{rated}} - U_{\mathrm{cut_{in}}}}, & U_{\mathrm{cut_{in}}} \leq U < U_{\mathrm{rated}}, \\ P_{\max}, & U_{\mathrm{rated}} \leq U < U_{\mathrm{cut_{out}}}. \end{cases} \quad (3)$$

To perform this calculation, basic turbine specifications are required, including the cut-in wind speed ($U_{\mathrm{cut_{in}}}$), rated wind speed ($U_{\mathrm{rated}}$), cut-out wind speed ($U_{\mathrm{cut_{out}}}$), and maximum rated power output ($P_{\max}$). In this study, we use $P_{\max} = 4700$ kW as the maximum rated power output. Values of 3, 13, and 25 $m \cdot s^{-1}$ are used for the cut-in, rated, and cut-out wind speeds, respectively, representing a typical onshore wind turbine installed in northern Germany in recent years (BWE, 2023; Lehneis *et al.*, 2021).

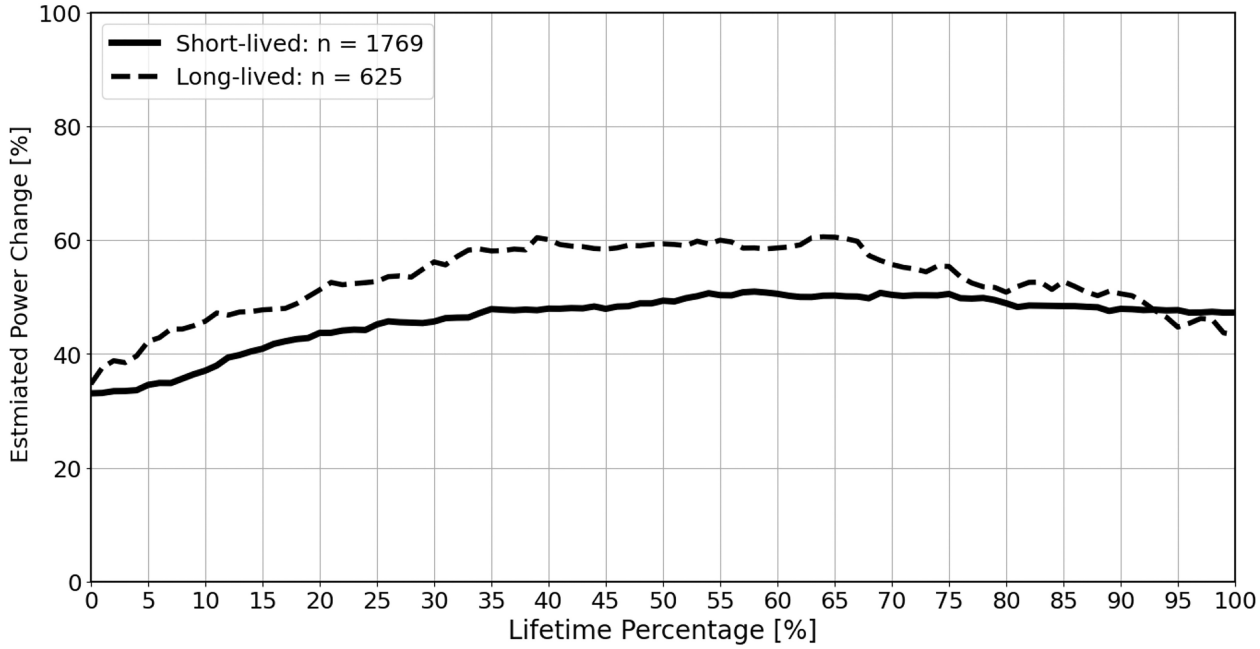


**FIGURE 10** Life-cycle evolution of median estimated power output increase (%), from the median mean wind-power output at 100 m, compared with the median power output associated with the maximum wind speed at 100 m.

Below the cut-in wind speed, the turbine does not generate power. Between the cut-in and rated wind speeds, power is assumed to increase linearly. At and above the rated wind speed, the turbine is assumed to operate at maximum output until it reaches the cut-out wind speed, beyond which it would shut down to prevent mechanical damage. This simplified power curve provides a reasonable estimate of wind power based solely on wind speed and is suitable for statistical analyses over extended simulation periods, as conducted in this study.

We estimate the potential power available in the flow field following a convective cell, in the absence of an actual turbine. The idea is to provide a rough estimate of what effects a cold-pool wind gust would have on power production at any given point in its life cycle. Estimated power output for the lifetime of a convective cell is shown for the 100-m mean (Figure 9e) and maximum (Figure 9f) wind speed. Power output associated with the mean wind speed is approximately constant throughout the cell life cycle, with the output falling below maximum output for the 10th–90th percentiles shown here.

When power output is estimated with the maximum wind speed, there is a clear increase in the median curves for both categories of cells, with similar timings of peak median values as for the maximum 100-m wind speed. A maximum power output of 4700 kW is attained by cells with wind speeds lying between the 50th and 90th percentiles (however, the power output in reality may be different when turbine operational adjustment like pitching or yawing is considered), and can be described as a downward-facing parabola for longer-lived cells. To quantify this increase in power in time between the median curves for mean and maximum 100-m power, Figure 10 shows the percentage increase in estimated power output between the median curves shown in Figure 9e,f. When considering the effects of the increased power output due to convective cold pools compared with the mean flow alone, there is an increase in power output of between 35% and 60% for longer-lived cells, with the largest increase in estimated power occurring about halfway through the cell life cycle. For smaller cells, the difference is slightly smaller, yet there is still an estimated increase of between 33% and 50% with a cold-pool passage. The estimated power output change is also often greater for longer-lived than for shorter-lived cells. For up to 75% of a longer-lived cell's lifetime, there is significantly more power output than shorter-lived cells (notably, the output is 10% greater between about one- and two-thirds of the way through a given cell's lifetime). This indicates not only that convective cold-pool gust fronts will likely increase power generation compared with the background flow, but that prediction of convective cell longevity could provide additional helpful guidance for short-term power forecasting.

## 6 | CONCLUSIONS

Deep convection and cold-pool characteristics over Germany for the month of July 2023 are analysed in both DWD

radar observations and a numerical simulation using the WRF model. The analysis is split into two main components: characteristics of convective snapshots produced at all times available and a Lagrangian framework, where isolated characteristics of convective cells are tracked in time to produce life cycles. For both components, the model is evaluated with DWD observations.

The WRF model captures the general distribution of deep convection and cold-pool-related characteristics over Germany reasonably well. However, it tends to simulate smaller, more intense rain-producing cells compared with DWD observations, a result that corroborates previous research on deep convection using WRF. A statistical tool (the Jensen–Shannon divergence metric) was used to quantify how similar the distributions are between model and observations. The results also show that, in particular, the distributions of convective shape, propagation speed, and direction show extremely high similarity. The distribution of mean reflectivity also shows high correlation with observations.

We also aimed to quantify the wind speeds, temperature, and temperature stratification change associated with simulated convective cold pools. Median cold-pool characteristics and associated wind gusts simulated by WRF align with observed values, including temperature differences and gust strengths (although, given the relative paucity of observations for these quantities, more extensive characteristics of ground-based observations are required for a more complete model evaluation). In particular, median values of about −3 K minimum $\theta_v$ difference in WRF closely match results from the FESSTVaL field campaign. Extreme temperature differences found in WRF are also close to the extreme values in observations (values of −10.8 K observed during FESSTVaL). While the median wind perturbations also match those found in observations (around 4.4 $m \cdot s^{-1}$), the model suggests that extreme wind perturbations exceeding 10 $m \cdot s^{-1}$ and large shear exponent values are possible, highlighting the potential for significant stress on wind turbines during cold-pool events. Depending on the strength of the background flow, how close that is to the turbine rated wind speed, and the amplitude of the wind gust, there can be significant increases in wind-power output and turbine loading (Kelly *et al.*, 2021). The vertical structure of the wind field and, in particular, the structure of vertical shear in these extreme cases warrants further investigation.

The temporal evolution of isolated convective cells is comparable in WRF and in DWD observations, with variables in WRF and observations often following a parabolic evolution in time. The evolution of cell size is downward-facing parabolic, with the largest size occurring halfway through the life cycle, a result found in both observations and WRF. These results corroborate a recent study using a nowcasting tool from DWD. While rain rate and mean reflectivity also have a downward-facing parabolic evolution with time, WRF intensifies cells too quickly compared with observations and rains too intensely throughout the life cycle. Cell shape, however, is remarkably consistent across simulation and observations for life cycles, with essentially no change found through life cycles for either shorter- or longer-lived cells.

The life-cycle analysis was extended to include wind-energy relevant model output. Life cycles of variables such as minimum 2-m $\theta_v$ differences, mean rotor-layer stability, maximum rotor-layer shear exponent, maximum wind speed, and estimated power output all show a parabolic evolution with time. There is an increasing atmospheric stabilization over the lifetime of the cell, which would impact the strength and duration of turbulent wakes. Stronger and longer-lasting turbine wakes produced within a cold pool would potentially impact downwind turbines in wind farms. Stabilization is highly correlated with an increase in wind shear and reduced turbulence, which causes changes in turbine loads throughout the wind farm (Wharton and Lundquist, 2011; Sathe *et al.*, 2013). Saturation deficit decreases over the lifetime of the cell, with falling rain progressively evaporating and moistening the sub-cloud layer.

A calculation of electrical power output is offered based on the crude estimate where the wind field is applied to a simplified power curve. A lifetime power estimate for mean and maximum power at 100 m is produced, which provides guidance as to how much increased power output would be expected when a cold pool traverses a wind turbine at any particular point in its life cycle. Power output increases dramatically for the generic turbine design described here when comparing the effects of the mean flow alone with those of the maximum wind perturbation, with power output increasing by 35%–60% for longer-lived cells and 33%–50% for shorter-lived cells. Power output peaks mid-life-cycle for longer-lived cells, or at about three-quarters of the life cycle for shorter-lived cells. The results also suggest that newly developed cells, which are the hardest to nowcast due to the stochastic nature of convective cell formation, produce the smallest increase in power output.

In reality, turbines at a fixed location would experience increases in winds and power output due to cold-pool passages over a roughly 20–30 minute period, where the ramp up from background flow to maximum wind takes between 5 and 10 minutes and the winds stay close to maximum for roughly 5 minutes (not shown). While these events are relatively short-lived, and occur only between 24 and 44 times per summer season, they are nonetheless important to understand in the context of minute-scale wind-power forecasting for energy trading, as the German

electrical grid operates on lead times down to 5 minutes (Würth *et al.*, 2019). Additionally, since the median size of an observed cold-pool-producing cell is 225.65 km$^2$, the associated cold-pool gust front would likely impact multiple turbines or potentially whole wind parks during its lifetime.

While the simulation results presented here in terms of cold pools appear broadly reasonable, it is important to emphasize that we are unable to validate cold-pool characteristics and associated wind-power output across the entire model domain, as we do for the parent convective cells. Given the limitations of observational coverage, particularly in areas away from surface-based instrumentation, we take care not to overstate the implications of our findings, especially in relation to wind-energy impacts. Validation against observational datasets is essential, especially considering known biases in WRF simulations. This step is critical for assessing the robustness of the modelled cold pools and their relevance for operational wind-energy applications. A companion study, aimed at quantifying the effects of observed cold-pool passages over a wind park, is currently in preparation, and in future work we plan to validate the wind-energy relevant model output with a ground-based observational network located at a wind park in northern Germany, where a meteorological mast has been erected and can offer insights into the vertical structure of the wind and vertical shear in cold pools up to a height of 150 m. The numerical model used here not only can be evaluated close to the ground, but also can be used to fill gaps in observations and offer a more complete understanding of the three-dimensional structure of cold pools impacting a wind park. To do that, a more robust method to detect and connect cold pools to their parent cells should also be defined.

A limitation of the current work is that, for the life cycles presented herein, the focus is purely on discrete or isolated convective elements that do not interact with neighbouring cells, or have not previously undergone a split or merge event. This decision would remove from the analysis, for example, larger mesoscale systems like squall lines, which are often related to intense cold pools. Supercells, while relatively uncommon, are the most dangerous form of convective cell, and would also not likely be included in the current analysis, as by definition a supercell forms from the splitting of an original cell into two oppositely propagating components (Rotunno & Klemp, 1985). Future work should also attempt to classify the effects of these potentially important phenomena in relation to wind-energy applications.

## ACKNOWLEDGMENTS

We are grateful to two anonymous reviewers for their thoughtful and thorough reviews of the original article. We acknowledge Douglas Uba, one of the creators of the TATHU algorithm, for helping us to modify the TATHU code to process our data. We also thank Dr Antonia Englberger and Dr Axel Lauer for their helpful comments on an earlier version of the article. This work used resources of the Deutsches Klimarechenzentrum (DKRZ) granted by its Scientific Steering Committee (WLA) under project ID bd1069. Open Access funding enabled and organized by Projekt DEAL.

## DATA AVAILABILITY STATEMENT

Raw radar data were generated at the German Weather Service (DWD) and are publicly available. For more information, visit https://www.dwd.de/EN/ourservices/opendata/opendata.html. The model data that support the findings of this study are available from the corresponding author upon reasonable request. The WRF model namelists used to produce the simulation in this study are publicly available on Zenodo at https://doi.org/10.5281/zenodo.16759999.

## ENDNOTE

[1]The density potential temperature $\theta_\rho$ is a type of potential temperature that accounts for the effect of water loading and is particularly useful in anelastic models to describe buoyancy.

## REFERENCES

Anisimov, A., Efimov, V., Lvova, M., Mostamandi, S. & Stenchikov, G. (2023) Cloud-resolving modeling and evaluation of microphysical schemes for flash flood–producing convection over the black sea. *Journal of Hydrometeorology*, 24, 835–851. Available from: https://doi.org/10.1175/JHM-D-22-0060.1

Benjamin, T.B. (1968) Gravity currents and related phenomena. *Journal of Fluid Mechanics*, 31, 209–248.

BMWK. (2024) Time series for the development of renewable energy sources in Germany based on statistical data from the Working Group on Renewable Energy-Statistics (AGEE-Stat) (Status: September 2024). Report, 25 pp. Available from: https://www.bmwk.de/Redaktion/DE/Downloads/Energie/zeitreihen-zur-entwicklung-der-erneuerbaren-energien-in-deutschland-1990-2023-en.pdf

Bryan, G.H. & Morrison, H. (2012) Sensitivity of a simulated squall line to horizontal resolution and parameterization of microphysics. *Monthly Weather Review*, 140, 202–225.

Bryan, G.H., Wyngaard, J.C. & Fritsch, J.M. (2003) Resolution requirements for the simulation of deep moist convection. *Monthly Weather Review*, 131, 2394–2416.

BWE. (2023) Status of onshore wind energy development in Germany year, 2023. Report. Available from: https://www.wind-energie.de/english/statistics/statistics-germany/

Canepa, F., Burlando, M. & Solari, G. (2020) Vertical profile characteristics of thunderstorm outflows. *Journal of Wind Engineering and Industrial Aerodynamics*, 206, 104332.

Cotton, W.R., Bryan, G. & Van den Heever, S.C. (2010) *Storm and cloud dynamics*, Vol. 99, 2nd edition. Amsterdam: Academic Press.

DeMarco, A. & Basu, S. (2018) On the tails of the wind ramp distributions. *Wind Energy*, 21(10), 892–905.

Drager, A.J. & van den Heever, S.C. (2017) Characterizing convective cold pools. *Journal of Advances in Modeling Earth Systems*, 9, 1091–1115. Available from: https://doi.org/10.1002/2016MS000788

Drew, D.R., Barlow, J.F. & Coker, P.J. (2018) Identifying and characterising large ramps in power output of offshore wind farms. *Renewable Energy*, 127, 195–203.

Droegemeier, K. & Wilhelmson, R. (1987) Numerical simulation of thunderstorm outflow dynamics. Part I: outflow sensitivity experiments and turbulence dynamics. *Journal of the Atmospheric Sciences*, 44(8), 1180–1210. Available from: https://doi.org/10.1175/1520-0469(1987)0442.0CO;2

Dudhia, J. (1989) Numerical study of convection observed during the winter monsoon experiment using a mesoscale two-dimensional model. *Journal of the Atmospheric Sciences*, 46, 3077–3107.

Englberger, A. & Doernbrack, A. (2018) Impact of the diurnal cycle of the atmospheric boundary layer on wind-turbine wakes: a numerical modelling study. *Boundary-Layer Meteorology*, 166, 423–448.

Fan, J., Han, B., Varble, A., Morrison, H., North, K., Kollias, P. et al. (2017) Cloud-resolving model intercomparison of an MC3E squall line case: Part I—convective updrafts. *Journal of Geophysical Research – Atmospheres*, 122, 9351–9378. Available from: https://doi.org/10.1002/2017JD026622

Feng, C. & Zhang, J. (2018) Wind power and ramp forecasting for grid integration. In: Hu, W. (Ed.) *Advanced wind turbine technology*. Cham: Springer International Publishing, pp. 299–315.

Fievet, R., Meyer, B. & Haerter, J.O. (2023) On the sensitivity of convective cold pools to mesh resolution. *Journal of Advances in Modeling Earth Systems*, 15, e2022MS003382.

Fraunhofer ISE. (2024) German Net Power Generation in FirstHalf of 2024: Record Generation of Green Power, Generation from Fossil Fuels Continues Decline. Available from: https://www.ise.fraunhofer.de/en/press-media/press-releases/2024/german-net-power-generation-in-first-half-2024-record-generation-of-green-power-generation-from-fossil-fuels-continues-decline.html

Fournier, M.B. & Haerter, J.O. (2019) Tracking the gust fronts of convective cold pools. *Journal of Geophysical Research: Atmospheres*, 124, 11103–11117. Available from: https://doi.org/10.1029/2019JD030980

Gallego, C., Cuerva-Tejero, A. & Lopez-Garcia, O. (2015) A review on the recent history of wind power ramp forecasting. *Renewable & Sustainable Energy Reviews*, 52, 1148–1157.

Goff, R.C. (1976) Vertical structure of thunderstorm outflows. *Monthly Weather Review*, 104(11), 1429–1440.

Goudenhoofdt, E. & Delobbe, L. (2013) Statistical Characteristics of Convective Storms in Belgium Derived from Volumetric Weather Radar Observations. *Journal of Applied Meteorology and Climatology*, 52, 918–934. Available from: https://doi.org/10.1175/JAMC-D-12-079.1

Grant, L.D., KirschJ, B., Bukowski, N.M., Falk, C.A., Neumaier, M., van den, S.C. et al. (2024) How variable are cold pools? *Geophysical Research Letters*, 51(6), e2023GL106784.

Grant, L.D. & van den Heever, S.C. (2016) Cold pool dissipation. *Journal of Geophysical Research: Atmospheres*, 121, 1138–1155. Available from: https://doi.org/10.1002/2015JD023813

Gunter, W.S. & Schroeder, J.L. (2015) High-resolution full-scale measurements of thunderstorm outflow winds. *Journal of Wind Engineering and Industrial Aerodynamics*, 138, 13–26. Available from: https://doi.org/10.1016/j.jweia.2014.12.005

Han, B., Fan, J., Varble, A., Morrison, H., Williams, C.R., Chen, B. et al. (2019) Cloud-Resolving model intercomparison of an MC3E squall line case: Part II. stratiform precipitation properties. *Journal of Geophysical Research: Atmospheres*, 124(2), 1090–1117.

Hirt, M., Craig, G.C., Schäfer, S.A.K., Savre, J. & Heinze, R. (2020) Cold-pool-driven convective initiation: using causal graph analysis to determine what convection-permitting models are missing. *Quarterly Journal of the Royal Meteorological Society*, 146, 2205–2227. Available from: https://doi.org/10.1002/qj.3788

Hoeller, J., Haerter, J.O. & Da Silva, N.A. (2024) Characteristics of station-derived convective cold pools over equatorial Africa. *Geophysical Research Letters*, 51, e2023GL107308.

Hohenegger, C., Ament, F., Beyrich, F., Löhnert, U., Rust, H., Bange, J. et al. (2023) FESSTVaL: the field experiment on submesoscale spatio-temporal variability in Lindenberg. *Bulletin of the American Meteorological Society*, 104, E1875–E1892.

Houze, R.A. (2014) *Cloud dynamics, international geophysics*, Vol. 104. Amsterdam: Academic Press, p. 432.

Jimenez, P.A., Dudhia, J., González-Rouco, J.F., Navarro, J., Montávez, J.P. & García-Bustamante, E. (2012) A revised scheme for the WRF surface layer formulation. *Monthly Weather Review*, 140, 898–918.

Kain, J.S. & Fritsch, J.M. (1993) Convective parameterization for mesoscale models: the Kain-Fritsch scheme. In: Emanuel, K.A. & Raymond, D.J. (Eds.) *the representation of cumulus convection in numerical models*. Meteorological monographs. Boston, MA: American Meteorological Society.

Kelly, M., Andersen, S.J. & Hannesdottir, Á. (2021) Statistical impact of wind-speed ramp events on turbines, via observations and coupled fluid-dynamic and aeroelastic simulations. *Wind Energy Science*, 6, 1227–1245. Available from: https://doi.org/10.5194/wes-6-1227-2021

Kelly, M., Larsen, G., Dimitrov, N.K. & Natarajan, A. (2014) Probabilistic meteorological characterization for turbine loads. *Journal of Physics: Conference Series*, 524, 012076.

Kirsch, B., Ament, F. & Hohenegger, C. (2021) Convective cold pools in long-term boundary layer mast observations. *Monthly Weather Review*, 149, 811–820.

Kirsch, B., Hohenegger, C. & Ament, F. (2024) Morphology and growth of convective cold pools observed by a dense station network in Germany. *Quarterly Journal of the Royal Meteorological Society*, 150(759), 857–876. Available from: https://doi.org/10.1002/qj.4626

Köcher, G., Zinner, T. & Knote, C. (2023) Influence of cloud microphysics schemes on weather model predictions of heavy precipitation. *Atmospheric Chemistry and Physics*, 23, 6255–6269.

Kruse, I.L., Haerter, J.O. & Meyer, B. (2022) Cold pools over the Netherlands: a statistical study from tower and radar observations. *Quarterly Journal of the Royal Meteorological Society*, 148, 711–726.

Lehneis, R., Manske, D. & Thran, D. (2021) Modeling of the German wind power production with high spatiotemporal resolution. *ISPRS International Journal of Geo-Information*, 10, 104. Available from: https://doi.org/10.3390/ijgi10020104

Lim, K.S. & Hong, S. (2010) Development of an effective double-moment cloud microphysics scheme with prognostic cloud condensation nuclei (CCN) for weather and climate models. *Monthly Weather Review*, 138, 1587–1612.

Lombardo, F.T., Smith, D.A., Schroeder, J.L. & Mehta, K.C. (2014) Thunderstorm characteristics of importance to wind engineering. *Journal of Wind Engineering and Industrial Aerodynamics*, 125, 121–132.

Min, K., Choo, S., Lee, D. & Lee, G. (2015) Evaluation of WRF cloud microphysics schemes using radar observations. *Weather and Forecasting*, 30, 1571–1589.

Mlawer, E.J., Taubman, S.J., Brown, P.D., Iacono, M.J. & Clough, S.A. (1997) Radiative transfer for inhomogeneous atmospheres: RRTM, a validated correlated-k model for the longwave. *Journal of Geophysical Research*, 102, 16663–16682.

Morrison, H., Thompson, G. & Tatarskii, V. (2009) Impact of cloud microphysics on the development of trailing stratiform precipitation in a simulated squall line: Comparison of one- and two-moment schemes. *Monthly Weather Review*, 137(3), 991–1007.

Niu, G.-Y., Yang, Z.-L., Mitchell, K.E., Chen, F., Ek, M.B., Barlage, M. et al. (2011) The community Noah land surface model with multiparameterization options (Noah-MP): 1. model description and evaluation with localscale measurements. *Journal of Geophysical Research: Atmospheres*, 116. Available from: https://agupubs.onlinelibrary.wiley.com/doi/epdf/10.1029/2010JD015139

Pacey, G.P., Schultz, D.M. & Garcia-Carreras, L. (2021) Severe convective windstorms in Europe: climatology, preconvective environments, and convective mode. *Weather and Forecasting*, 36, 237–252. Available from: https://doi.org/10.1175/WAF-D-20-0075.1

Pandey, A., Lamraoui, F., Smith, J.B., Clapp, C.E., Sayres, D.S. & Kuang, Z. (2023) Sensitivity of deep convection and cross-tropopause water transport to microphysical parameterizations in WRF. *Journal of Geophysical Research: Atmospheres*, 128, e2022JD037 053.

Parker, D.J. (1996) Cold pools in shear. *Quarterly Journal of the Royal Meteorological Society*, 122, 1655–1674.

Pichault, M., Vincent, C., Skidmore, G. & Monty, J. (2022) LiDAR-based detection of wind gusts: an experimental study of gust propagation speed and impact on wind power ramps. *Journal of Wind Engineering and Industrial Aerodynamics*, 220, 104864. Available from: https://doi.org/10.1016/J.JWEIA.2021.104864

Prein, R.M., Rasmussen, D.W. & Giangrande, S.E. (2021) Sensitivity of organized convective storms to model grid spacing in current and future climates. *Philosophical Transactions of the Royal Society*, A379, 20190546.

Pryor, S.C., Letson, F., Shepherd, T. & Barthelmie, R.J. (2023) Evaluation of WRF simulation of deep convection in the U.S. Southern great plains. *Journal of Applied Meteorology and Climatology*, 62, 41–62. Available from: https://doi.org/10.1175/JAMC-D-22-0090.1

Putnam, B.J., Xue, M., Jung, Y., Zhang, G. & Kong, F. (2016) Simulation of polarimetric radar variables from 2013 CAPS spring experiment storm-scale ensemble forecasts and evaluation of microphysics schemes. *Monthly Weather Review*, 145(1), 49–73.

Rotunno, R. & Klemp, J. (1985) On the rotation and propagation of simulated supercell thunderstorms. *Journal of the Atmospheric Sciences*, 42, 271–292.

Sathe, A., Mann, J., Barlas, T., Bierbooms, W.A.A.M. & van Bussel, G.J.W. (2013) Influence of atmospheric stability on wind turbine loads. *Wind Energy*, 16, 1013–1032. Available from: https://doi.org/10.1002/we.1528

Schütze, H. & Manning, C.D. (1999) *Foundations of statistical natural language processing*. Cambridge, MA: MIT Press, p. 304.

Sena, R.G., Negri, M.L. & Gava, L.M. (2024) GOES ABI-derived hailstorm polygons and tracking dataset for Brazil. *Data in Brief*, 55, 110736.

Skamarock, W.C., Klemp, J.B., Dudhia, J., Gill, D.O., Liu, Z., Berner, J. et al. (2021) *A description of the advanced research WRF model version 4*. Boulder, CO: National Center for Atmospheric Research.

Song, H.J. & Sohn, B.J. (2018) An evaluation of WRF microphysics schemes for simulating the warm-type heavy rain over the Korean Peninsula. *Asia-Pacific Journal of Atmospheric Sciences*, 54, 225–236.

Squitieri, B.J. & Gallus, W.A. (2020) On the forecast sensitivity of MCS cold pools and related features to horizontal grid spacing in convection-allowing WRF simulations. *Weather and Forecasting*, 35, 325–346. Available from: https://doi.org/10.1175/WAF-D-19-0016.1

Steiner, A., Köhler, C., Metzinger, I., Braun, A., Zirkelbach, M., Ernst, D. et al. (2017) Critical weather situations for renewable energies – Part A: cyclone detection for wind power. *Renewable Energy*, 101, 41–50. Available from: https://doi.org/10.1016/j.renene.2016.08.013

Straka, J.M., Wilhelmson, R.B., Wicker, L.J., Anderson, J.R. & Droegemeier, K.K. (1993) Numerical solutions of a non-linear density current: a benchmark solution and comparisons. *International Journal for Numerical Methods in Fluids*, 17(1), 1–22. Available from: https://doi.org/10.1002/fld.1650170103

Thompson, G., Field, P.R., Rasmussen, R.M. & Hall, W.D. (2008) Explicit forecasts of winter precipitation using an improved bulk microphysics scheme. Part II: Implementation of a new snow parameterization. *Monthly Weather Review*, 136(12), 5095–5115.

Uba, D.M., Negri, R.G., Enoré, D.P., Costa, I.C. & Jorge, A.A.S. (2022) TATHU - software para rastreio e análise do ciclo de vida de sistemas convectivos. São José dos Campos: INPE. 39 p. IBI: <8JMKD3MGP3W34T/47AF772>.

Wagner, A., Heinzeller, D., Wagner, S., Rummler, T. & Kunstmann, H. (2018a) Explicit convection and scale-aware cumulus parameterizations: high-resolution simulations over areas of different topography in Germany. *Monthly Weather Review*, 146, 1925–1944. Available from: https://doi.org/10.1175/MWR-D-17-0238.1

Wagner, J., Gerz, T., Wildmann, N. & Gramitzky, K. (2018b) Long-term simulation of the boundary layer flow over the double-ridge site during the Perdigão 2017 field campaign. *Atmospheric Chemistry and Physics*, 19, 1129–1146.

Wapler, K. (2021) Mesocyclonic and non-mesocyclonic convective storms in Germany: storm characteristics and life-cycle. *Atmospheric Research*, 248, 105186.

Wharton, S. & Lundquist, J.K. (2011) Assessing atmospheric stability and its impacts on rotor-disk wind characteristics at an onshore wind farm. *Wind Energy*, 15, 525–546. Available from: https://doi.org/10.1002/we.483

Wildmann, N., Hagen, M. & Gerz, T. (2022) Enhanced resource assessment and atmospheric monitoring of the research wind farm WiValdi. *Journal of Physics: Conference Series*, 2265(2),

022029. Available from: https://doi.org/10.1088/1742-6596/2265/2/022029

Wilhelm, J., Wapler, K., Blahak, U., Potthast, R. & Kunz, M. (2023) Statistical relevance of meteorological ambient conditions and cell attributes for nowcasting the life cycle of convective storms. *Quarterly Journal of the Royal Meteorological Society*, 149(755), 2252–2280.

Wilhelmson, R.B. & Wicker, L.J. (2001) Numerical modeling of severe local storms. In: *Severe convective storms, meteorological monographs*, Vol. 50. Boston, MA: American Meteorological Society, pp. 123–166. Available from: https://doi.org/10.1175/0065-9401-28.50.123

Wise, A.S., Arthur, R.S., Abraham, A., Wharton, S., Krishnamurthy, R., Newsom, R. et al. (2024) Large-eddy simulation of an atmospheric bore and associated gravity wave effects on wind farm performance in the southern great plains. *Wind Energy Science*, 10, 1007–1032.

Würth, I., Valldecabres, L., Simon, E., Möhrlen, C., Uzunoğlu, B., Gilbert, C. et al. (2019) Minute-scale forecasting of wind power—results from the Collaborative Workshop of IEA Wind Task 32 and 36. *Energies*, 12(4), 712. Available from: https://doi.org/10.3390/en12040712

Zhang, X., Bao, J.W., Chen, B. & Grell, E.D. (2018) A three-dimensional scale-adaptive turbulent kinetic energy scheme in the WRF-ARW model. *Monthly Weather Review*, 146, 2023–2045.

Zhou, A., Zhao, K., Lee, W.-C., Ding, Z., Lu, Y. & Huang, H. (2022) Evaluation and modification of microphysics schemes on the cold pool evolution for a simulated bow echo in southeast China. *Journal of Geophysical Research: Atmospheres*, 127, e2021.

Zipser, E.J. (1969) The role of organized unsaturated convective downdrafts in the structure and rapid decay of an equatorial disturbance. *Journal of Applied Meteorology*, 8, 799–814.

**How to cite this article:** Kilroy, G. & Thayer, J.D. (2025) Evaluation of the WRF model for simulating deep convection and cold-pool characteristics relevant to wind-energy applications in Germany. *Quarterly Journal of the Royal Meteorological Society*, e70042. Available from: https://doi.org/10.1002/qj.70042